Lithos 208–209 (2014) 202–219

Contents lists available at ScienceDirect

Lithos

journal homepage: www.elsevier.com/locate/lithos

Petrogenesis of Late Cretaceous I-type granites in the southern Yidun Terrane: New constraints on the Late Mesozoic tectonic evolution of the eastern Tibetan Plateau

Xin-Song Wang [a,b], Rui-Zhong Hu [a], Xian-Wu Bi [a,*], Cheng-Biao Leng [a], Li-Chuan Pan [a,b], Jing-Jing Zhu [a], You-Wei Chen [a]

[a] State Key Laboratory of Ore Deposits Geochemistry, Institute of Geochemistry, China Academy of Sciences, Guiyang 550005, China
[b] University of Chinese Academy of Sciences, Beijing 100049, China

ARTICLE INFO

Article history:
Received 22 December 2013
Accepted 27 August 2014
Available online 19 September 2014

Keywords:
Granites
Sr–Nd–Hf–O isotopes
Meso-Tethys
Yidun terrane
Eastern Tibetan Plateau

ABSTRACT

The collision between the Lhasa and Qiangtang terranes, prior to the Indo–Asian collision, is a critical aspect in terms of development of the Tibetan Plateau. It has been demonstrated that the occurrence of the Late Cretaceous granites (110–80 Ma) in the Yidun Terrane, eastern Tibetan Plateau (ETP) associates with the Lhasa–Qiangtang collision. The Xiuwacu Late Cretaceous pluton in the southern Yidun Terrane, consists three phases including biotite granitic porphyry (phase 1), monzogranite (phase 2), and alkali–feldspar leucogranite (phase 3), which have zircon U–Pb ages ranging from 85.5 Ma to 84.4 Ma. All these three phases are metaluminous or slightly peraluminous granites (A/CNK = 0.96–1.07), with high SiO_2 (70.0–76.0 wt.%), $K_2O + Na_2O$ (7.5–10.7 wt.%), and Ga/Al (2.5–4.7), and relatively low CaO (0.39–1.67 wt.%), MgO (0.01–0.57 wt.%), and P_2O_5 (0.01–0.17 wt.%). The granites are enriched in light rare earth elements (LREEs), Rb, Th, U and Ta, but depleted in heavy REEs (HREEs), Ba, Sr, P, and Ti, with significantly negative Eu anomalies ($Eu/Eu^* = 0.24–0.59$). Comparing to classic A-type granites, these samples present higher Sr (10.1–256 ppm, mostly >100 ppm) and lower FeO*/MgO ratios (1.2–9.9) and Zr + Nb + Ce + Y (248–483 ppm, mostly <350 ppm). However, they show highly fractionated I-type granites affinities. All these phases have relatively high $(^{87}Sr/^{86}Sr)_i$ (0.7075–0.7098), negative $\varepsilon_{Nd}(t)$ (−8.0 to −6.9) and $\varepsilon_{Hf}(t)$ (−7.6 to −3.2) values, and ancient Nd and Hf model ages (1.7–1.3 Ga), which indicates similar origins predominately through partial melting of ancient mafic-intermediate lower continental crust. Besides, variable zircon $\delta^{18}O$ values (5.9‰ to 8.4‰, partly < 6.5‰) and the occurrences of mafic microgranular enclaves (MMEs) within the granites probably indicate a contribution of mantle components. Although the Xiuwacu Late Cretaceous intrusions show higher SiO_2 values and lower Sr/Y ratios comparing to other three high Sr/Y I-type intrusions (Relin, Hongshan, and Tongchanggou) in the southern Yidun Terrane, similar $(^{87}Sr/^{86}Sr)_i$, $\varepsilon_{Nd}(t)$, $\varepsilon_{Hf}(t)$, and $\delta^{18}O$ contents in all of these four intrusions point to a common source. We propose that both the Xiuwacu intrusions and the other three intrusions in the southern Yidun Terrane were generated under a late- or post-collision environment related to the Lhasa–Qiangtang collision during the Late Cretaceous. Decompression induced upwelling of mantle-derived magmas to underplate and provided heat for the anatexis of thickened lower crust. Then, those Late Cretaceous magmas were brought into the southern Yidun Terrane by mixing of lower continental crust-derived melts and minor mantle-derived magmas, and the following fractional crystallization. Occurrence of these late- or post-collision magmas probably indicates that the timing of both the Lhasa–Qiangtang collision and the eastern Tibetan Plateau uplifting was earlier than the Late Cretaceous, and that the Lhasa–Qiangtang collision did not cease at least until ca. 80 Ma. Afterwards, tectonic setting of the eastern Tibetan Plateau was progressively to be under a control mainly of the subduction of the Neo-Tethys Ocean and subsequent Indo–Asian collision.

1. Introduction

Although crustal recycling, i.e., remelting of preexisting supracrustal sedimentary rocks or infracrustal igneous rocks, seems to control the composition of majority granites (Chappell and White, 1992, 2001), it is also widely suggested that mantle-derived magmas play a significant role in providing heat and/or mass input (Kemp et al., 2007; Li et al.,

* Corresponding author. Tel.: +86 851 589 1962; fax: +86 851 5891664.
E-mail addresses: wangxinsong@mail.gyig.ac.cn (X.-S. Wang), bixianwu@vip.gyig.ac.cn (X.-W. Bi).

http://dx.doi.org/10.1016/j.lithos.2014.08.016
0024-4937/

2007; Yang et al., 2004; Zhong et al., 2009). Highly fractionated I-type granites consist pervasively of multi-phases with several stages of magmatisms (Li et al., 2009b; Whalen et al., 1987; Wu et al., 2003a; Zhu et al., 2009b). It is of first importance to understand if the component changes of those phases are related to additional contributions from mantle melts or from crustal materials during fractional crystallization processes. Those processes could not be easily recognized through traditional approaches (Li et al., 2009b), because the Sr and Nd isotopic compositions likely trend to be homogenous during the mixing between mafic and felsic magmas (Yang et al., 2006). However, newly developed in situ zircon Hf–O isotopic analysis provides an effective constraint on tracing the involvement of supracrustal materials or mantle-derived magma in granite genesis (Griffin et al., 2002; Kemp et al., 2005, 2007).

The surface uplift history of the Tibetan Plateau has been among the most interesting topics in geosciences because of its significance in changing not only Cenozoic regional climate but also large scale atmospheric circulations such as the Asian monsoon intensity (Wang et al., 2008a; Zhang et al., 2012; Zhu et al., 2013). It has long been recognized that the collision between the Lhasa Terrane and Qiangtang Terrane is, prior to the Indo–Asian collision, critical aspect in development of the Tibetan Plateau (Murphy et al., 1997; Sengor, 1979, 1987), however, any conclusions regarding when did the Bangong Meso-Tethys Ocean close and how long did the Lhasa–Qiangtang collision last remain open to intense debate. Murphy et al. (1997) proposed that significant crustal thickening caused by the Lhasa–Qiangtang collision occurred during the Early Cretaceous. Later researches suggested that the Lhasa–Qiangtang collision occurred during the Cretaceous (Kapp et al., 2005, 2007; Yin and Harrison, 2000), and that significant shortening of the Lhasa Terrane occurred during the Late Cretaceous (Guynn et al., 2006; Kapp et al., 2003; Zhu et al., 2011a, 2013). Additionally, Zhang et al. (2012) suggested that the Bangong Meso-Tethys did not close and the Qiangtang Terrane did not collide with the Lhasa Terrane until the Late Cretaceous. Generally, previous models mostly focused on data from the interior of central Tibet (Wang et al., 2008a), and were seldom constrained by geologic data from the eastern Tibetan Plateau. The Yidun Terrane, which is located on the eastern margin of the Qiangtang Terrane (Fig. 1a), is notable for its large-scale distribution of Late Cretaceous intrusions (110–80 Ma) along the north–south strike (Fig. 1b; Hou et al., 2003; Hou and Zhou, 2001). Although our earlier study demonstrated that these intrusions were genetically related to the Lhasa–Qiangtang collision (Wang et al., 2014), further studies on their petrogenesis and geodynamic setting would give additional constrains on the tectonic evolution of the eastern Tibetan Plateau (ETP) during Late Cretaceous.

In this study, we investigated the Xiuwacu Late Cretaceous multiphases pluton in the southern Yidun Terrane. Zircon Hf and O isotopic, whole-rock Sr–Nd isotopic, geochemical, and mineralogical compositions were analyzed for each phase of the Late Cretaceous intrusions to better understand the petrogenesis of the Xiuwacu pluton. In addition, new zircon Hf–O isotopic, whole-rock Sr–Nd isotopic, and mineralogical data of other Late Cretaceous intrusions (Relin, Hongshan, and Tongchanggou) in the southern Yidun Terrane were also achieved to constrain their petrogenesis and geodynamic setting.

2. Regional geology

The Tibetan Plateau is the most extensive region of elevated topography in the world. The eastern Tibetan Plateau is generally composed of the West Songpan–Ganzi Fold Belt, West Sichuan Basin, the Yidun Terrane and West Yunnan (Fig. 1a; Wilson and Fowler, 2011; Xu and Kamp, 2000). The uplifting of the Tibetan Plateau is generally considered to have been related to the Lhasa–Qiangtang collision during the Late Mesozoic and the Indo–Asian collision during the Late Cenozoic (Murphy et al., 1997; Wang et al., 2008). The Bangong–Nujiang Suture is the northern branch of the Meso-Tethys between the Lhasa and Qiangtang terranes (Metcalfe, 2011; Morley, 2012). The geological evolution of the Bangong–Nujiang Suture Zone (BNSZ) remains intensely debated. Some researchers proposed a northward subduction (Kapp et al., 2005, 2007; Zhang et al., 2012), whereas others suggested a south-dipping slab (Sui et al., 2013; Zhu et al., 2009b, 2011a). A bidirectional subduction model has also been presented in many studies (Du et al., 2011; Pan et al., 2012; Qu et al., 2012). Although the subduction direction of the Bangong Meso-Tethys Ocean remains controversial, most researchers suggested that the Lhasa Terrane initially collided with the Qiangtang Terrane during the Late Jurassic and Early Cretaceous (earlier in the east and later in the west), the premise of which is supported by stratigraphy and sedimentology studies along the BNSZ (Kapp et al., 2005, 2007; Zhu et al., 2011a, 2013). In addition, slab break-off probably developed during the Early Cretaceous (~113 Ma) after the initial collision (Zhu et al., 2011a). However, Zhang et al. (2012) suggested that the Bangong Meso-Tethys Ocean did not close and the Qiangtang Terrane did not collide with the Lhasa Terrane until the Late Cretaceous (~80 Ma); these remarks were based on the discovery of 132–108 Ma aged ophiolites in central Tibet that contained abundant Middle Cretaceous radiolarians.

The Yidun Terrane lies between the Qiangtang Terrane (west), Songpan–Ganzi Fold Belt (northeast) and Yangtze Craton (southeast), and it is bounded to the west by the Jinshajiang Suture and to the east by the Ganzi–Litang Suture (Fig. 1a and b; Yin and Harrison, 2000). In addition, the Yidun Terrane is located on the eastern side of the Bangong Suture. It is composed of two parts: the Zhongza Massif (the western Yidun Terrane) and the eastern Yidun Terrane (Reid et al., 2005b). The Zhongza Massif is composed of carbonate-rich Paleozoic metasedimentary rocks intercalated with mafic volcanic rocks (Chang, 1997). Some researchers inferred that the Zhongza Massif is a 'microcontinent' that separated from the Yangtze Craton in the Late Permian during the opening of the Ganzi–Litang Ocean. This is supported by the following three lines of evidence. First, these Paleozoic metasedimentary rocks have fossil assemblages similar to the sediments of the western Yangtze Craton (Chang, 1997). Second, the Triassic volcanic rocks in the eastern Yidun Terrane show geochemical affinities with the continental arc volcanics (Hou et al., 2003; Leng et al., 2014; Mo et al., 2001). Finally, some inherited zircons with ancient ages from the Triassic igneous rocks in the eastern Yidun Terrane are correlated with the Yangtze Craton (Leng et al., 2014; Reid et al., 2007; Wang et al., 2013a). The eastern Yidun Terrane is composed of north–south extending Late Triassic volcanic–sedimentary successions and Late Triassic granitoids formed by the westward subduction of the Ganzi–Litang Ocean crust (Hou and Zhou, 2001; Leng et al., 2012; Wang et al., 2011a). The occurrence of Jurassic granites in the Yidun Terrane and Songpan–Ganzi Fold Belt is generally considered to be an indicator of a post-orogenic environment after the collision event between the two terranes (Table 1; Hu et al., 2005; Qu et al., 2003; Wang et al., 2008b; Zhao et al., 2007).

3. Petrography and sampling

Late Cretaceous intrusions are widely distributed along the north–south strike in the Yidun Terrane (Table 1; Fig. 1b). These intrusions mainly comprise biotite granite, biotite monzogranite, and granitic porphyry. Previous studies have suggested that intrusions in the northern Yidun Terrane are A-type granites with their ages ranging from 115 Ma to 75 Ma (Table 1; Hou and Zhou, 2001; Hou et al., 2003, 2004; Qu et al., 2002; Zhang, 1994; Zhang and Zhang, 1993), and that in the southern Yidun Terrane there are four contemporaneous (87–81 Ma) intrusions (Wang et al., 2014; Table 1), i.e., the Xiuwacu, Relin, Hongshan, and Tongchanggou intrusions (Fig. 1c). Expect for the Xiuwacu, the Relin, Hongshan, and Tongchanggou intrusions are I-type granites with high Sr/Y and La/Yb ratios showing adakite-like affinities (Wang et al., 2014).

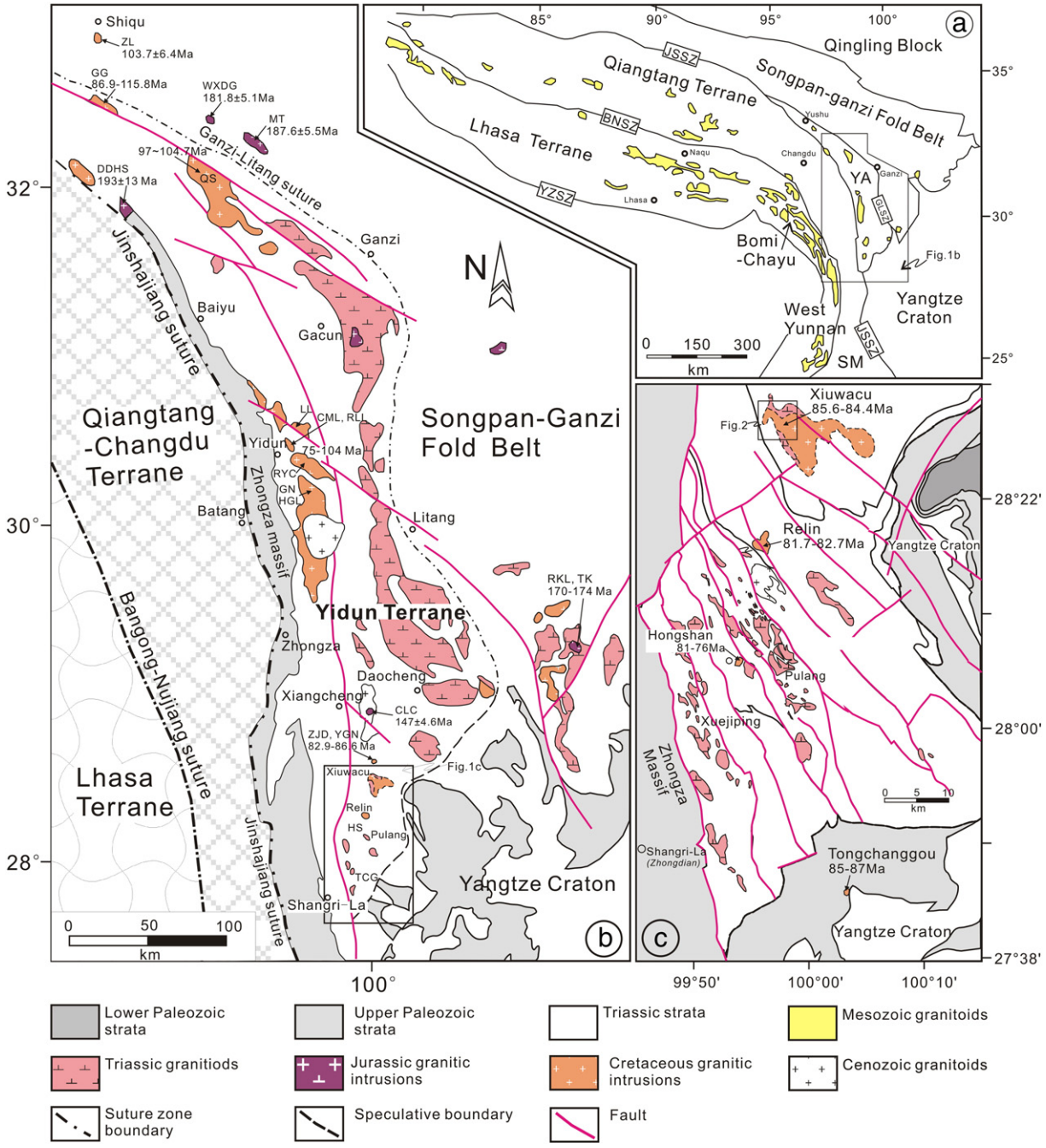

Fig. 1. (a) Regional location map showing terranes and Mesozoic granitoids in the Tibetan Plateau (Zhang et al., 2012; Zhu et al., 2011a); (b) Simplified geological maps of the Yidun Terrane (modified after Hou et al., 2007); (c) Simplified geological map of the Shangri-La region (modified after an unpublished geological map from the Yunnan Bureau of Geological Survey). Abbreviations: JSSZ = Jinsha Suture Zone; GLSN = Ganzi–Litang Suture Zone; BNSZ = Bangong–Nujiang Suture Zone; YZSZ = Yarlung–Zangbo Suture Zone; YA = Yidun Terrane (or Yidun Arc); SM = Simao Terrane; ZL = Zhalong intrusion; GG = Gaogong intrusion; WXDG = Waxu intrusion; MT = Mata intrusion; QS = Queershan intrusion; DDHS = Housa intrusion; LL = Lianlong intrusion; CML = Cuomolong intrusion; RLL = Ruoluolong intrusion; RYC = Rongyicuo intrusion; GN = Genie; HGL = Hagela (or Haizi); CLC = Cilincuo intrusion; ZJD = Zhujiding intrusion; YGN = Yigongnuo intrusion; HS = Hongshan intrusion; TCG = Tongchanggou intrusion; RKL = Rikulu intrusion; TK = Taka intrusion.
The ages of the intrusions are from Qu et al. (2002), Reid et al. (2007), Wang et al. (2008c), (2011b), (2014), Ying et al. (2006), Zhang (1994), and Zhang and Zhang (1993) and partly listed in Table 1.

The Xiuwacu pluton is located 80 km to the northeast of Shangri-La (Zhongdian) City (Fig. 1c). The Xiuwacu pluton is a complex with two stages of granitic intrusions including Late Triassic medium–coarse grained hornblende biotite monzogranite and Late Cretaceous granites (Fig. 2). Based on our field observations, the Xiuwacu Late Cretaceous granites can be divided into three phases: phase 1, early biotite granitic porphyry (Fig. 3a and d); phase 2, later medium–coarse grained monzogranite (Fig. 3b and e); and phase 3, final medium-fine grained alkali–feldspar leucogranite (Fig. 3c and f). The phase 2 has a gradational rather than clear contact with phase 1 (Fig. 3g) indicating that both of them were still un-solidified with high temperature when contacting with each other. The phase 3, intruding into the phase 1 and phase 2, generally has minor disseminated or veinlet-type molybdenite mineralization (Re–Os ages: 83 ± 1 Ma; Li et al., 2007). Furthermore, large quartz veins (20–100 m wide), K–Na feldspar, and fluorite megacrysts (3–20 cm) are found at depth under the phase 3 within the northern Xiuwacu block (Fig. 2b). Our previous zircon U–Pb dating suggested that they formed at 85.5–84.4 Ma (Table 1; Wang et al., 2014). The early biotite granitic porphyry, gray medium–coarse grained, consists of about 1–5% amphibole, 20% K-feldspar, 35% plagioclase, 25% quartz,

Table 1
Zircon LA–ICP-MS U–Pb ages of the Late Cretaceous and Jurassic granites in the Yidun Terrane.

	Intrusions	Sample. no	GPS position/location		Rock type	Ages (Ma)	±2σ	References
Southern Yidun Terrane	Xiuwacu phase 1	SXWC10-09	N28.496	E99.97	Biotite granitic porphyry	85.6	0.5	Wang et al. (2014)
	Xiuwacu phase 2	SXWC10-29	N28.498	E99.961	Monzogranite	84.8	0.6	Wang et al. (2014)
	Xiuwacu phase 3	XWC10-04	N28.505	E99.97	Alkali–feldspar leucogranite	84.4	1.4	Wang et al. (2014)
	Relin	RL10-09	N28.29	E99.939	Monzogranitic porphyry	82.7	0.5	Wang et al. (2014)
	Hongshan	HS10-03	N28.122	E99.877	Granitic porphyry	81.1	0.5	Wang et al. (2011)
	Hongshan	HS800	Hongshan, Shangri-La		Granitic porphyry	75.8	1.3	Huang et al. (2012)
	Tongchanggou	TCG10-11	N27.725	E100.076	Biotite granitic porphyry	87.4	0.6	Wang et al. (2014)
	Tongchanggou	TCG10-14	N27.739	E100.075	Biotite granitic porphyry	86.3	0.6	Wang et al. (2014)
Northern Yidun Terrane	Queershan	426	N31.94	E98.3	Biotite granite	104.7	2	Reid et al. (2007)
	Haizi	Ya32	N30.26	E99.44	Biotite granite	94.4	2.4	Reid et al. (2007)
	Niangbuke	rπtw	Ezhi, Dege		Biotite monzogranite	96.6	5.8	Wang et al. (2008b)
	Genie	TM1	Yidun, Batang		Biotite monzogranite	104.5	2.4	Wang et al. (2008b)
	Yigongnuo	YM16	Daocheng		Fine granite	86.6	3.3	Wang et al. (2008b)
	Zhujiding	ZJDB2	Daocheng		Fine quartz monzogranite	82.9	2.1	Wang et al. (2008b)
	Waxu	3195	Waxu, Dege		Diorite	181.8	5.1	Wang et al. (2008b)
	Rikulu	JL1	Rikulu, Jiulong		Biotite monzogranite	170.7	7.9	Wang et al. (2008b)
	Taka	JL9	Taka, Jiulong		Biotite monzogranite	174	11	Wang et al. (2008b)
	Housa	874TW	Dedeng, Jiangda		Biotite monzogranite	193	13	Wang et al. (2008b)
	Dongcuo	Da6	Danadeng, Litang		Biotite monzogranite	175	12	Wang et al. (2008b)
	Mata	V7H	Danadeng, Litang		Biotite monzogranite	187.5	5.5	Wang et al. (2008b)

10–15% biotite, and accessory minerals including zircon, apatite, magnetite, titanite, and ilmenite. The later monzogranite is pale red medium–coarse grained with about 30% K-feldspar, 30% plagioclase, 35% quartz, 3–5% biotite, 1% fluorite, and accessory minerals including zircon, apatite, magnetite, titanite, allanite, and ilmenite. The final alkali–feldspar leucogranite, medium-fine grained, consistent of about 40% K-feldspar, 30% plagioclase, 30% quartz, 1–3% biotite, 1% fluorite, and accessory minerals including zircon, apatite, monazite, rutile, thorite, and fergusonite. In addition, mafic microgranular enclaves (MMEs) are widely found in the two earlier phases, which have a clear or blurry contact with the host rocks and variable sizes (2–10 cm) (Fig. 3h). In contrast, some angular fragments of the sandstone from the strata instead of MMEs are found in the final alkali–feldspar leucogranite. Those angular fragments also have variable sizes (5–35 cm) and clear contact with the leucogranite. The strata in this district comprise Late Triassic medium-layered sandstone and slate. In addition, quartz-vein-type, greisens-type, and altered granite-type mineralization are developed in the Xiuwacu area. The ore bodies, enclosed by granites, extend northwest along regional faults. In this study, most samples were collected along the XY section with an altitudinal difference of about 400 m, covering the three different phases (Fig. 2). Other samples were also collected around the Xiuwacu area. All the granitic samples were relatively fresh, except for minor feldspar that had been altered to sericite locally.

The other three Late Cretaceous intrusions are located south of the Xiuwacu pluton in the Shangri-La region in the southern Yidun Terrane (Fig. 1b and c). Relin intrusion is gray medium–coarse grained monzogranitic porphyry with about 25–30% K-feldspar, 30–40% plagioclase, 30–35% quartz, and 3–5% biotite. The Hongshan intrusion, granitic porphyry, consists of 25–35% K-feldspar, 30–40% plagioclase, 30–35% quartz, 3–5% biotite, and 1–3% amphibole. The Tongchanggou intrusion is biotite granitic porphyry composed of 25–35% K-feldspar, 30–40% plagioclase, 25–30% quartz, and 5–10% biotite. Accessory minerals in these intrusions mainly include zircon, apatite, magnetite, titanite, and ilmenite.

4. Samples and analytical methods

4.1. Mineral composition analyses

Chemical composition analyses on plagioclase and biotite from all four intrusions were conducted using wavelength-dispersive X-ray

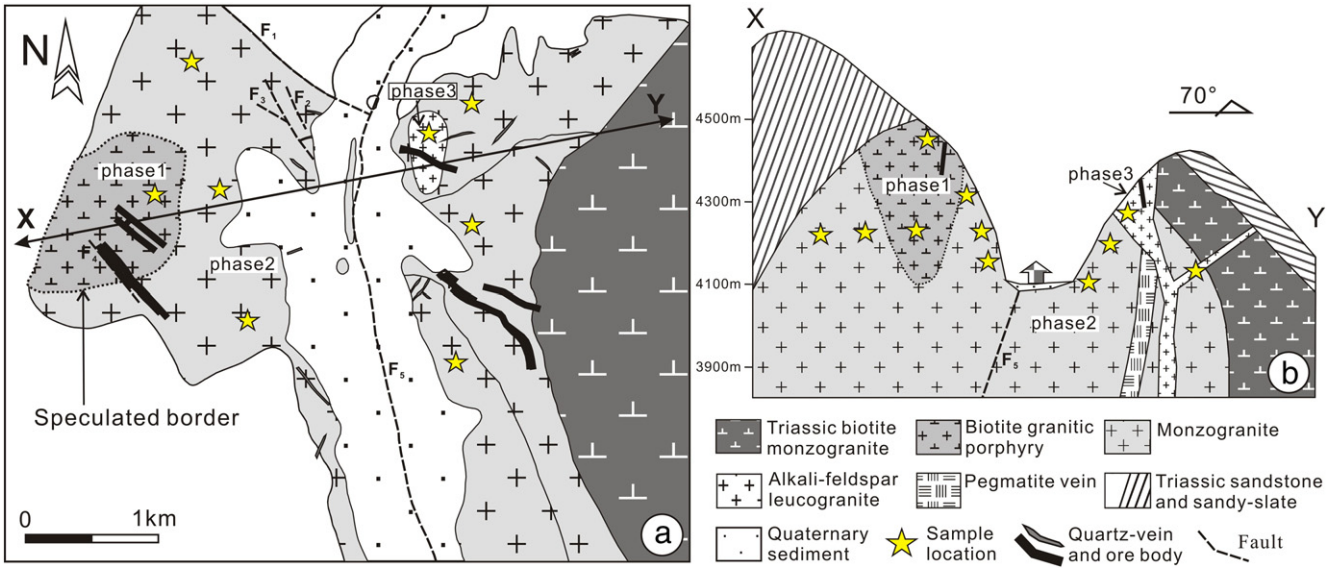

Fig. 2. Simplified geological map (a) and cross-section map (b) of the Xiuwacu pluton in the Xiuwacu area (modified after an unpublished exploration report from the Department of Land Resources, Yunnan Province, 1991). The boundary between the phase 1 and phase 2 is speculative boundary.

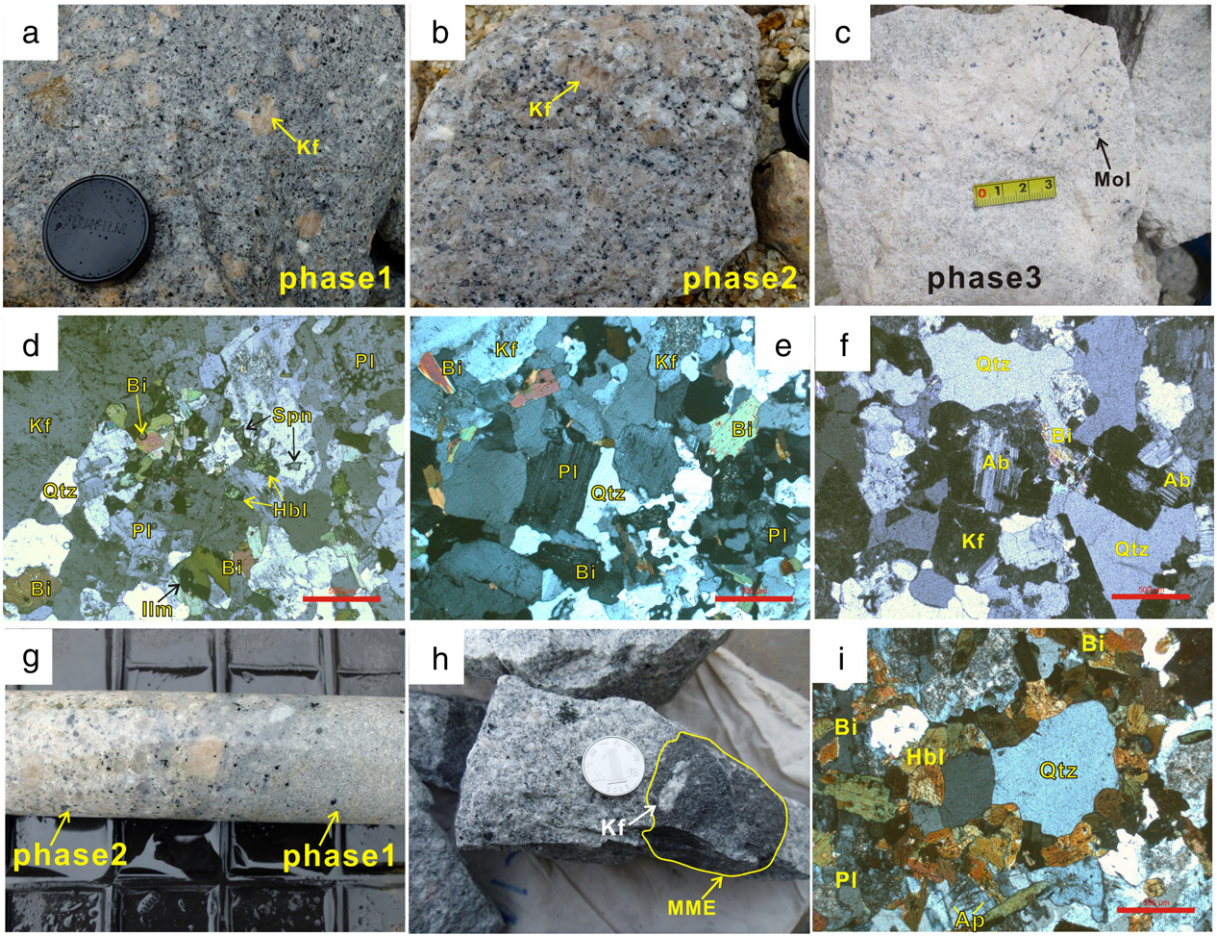

Fig. 3. Field photographs and photomicrographs of intrusions in the Xiuwacu area. (a) and (d) Phase 1 biotite granitic porphyry; (b) and (e) phase 2 medium–coarse grained monzogranite; (c) and (f) phase 3 medium-fine grained alkali–feldspar leucogranite with minor molybdenite mineralization; (g) phase 1 blurry contact with phase 2 indicating magmas of phase 2 intruding into un-solidified phase 1 and they have similar ages; (h) mafic microgranular enclaves (MMEs) in phase 1 biotite granitic porphyry with round edges K-feldspar megacrysts; (i) cross-polarized light of the ring structure from the MME in phase 1 that show typical ocellar texture with spheric shape, corrosion embayments, and hornblende and biotite mantle. Abbreviations of minerals: Kf — K-feldspar, Mol — molybdenite, Bi — biotite, Hbl — amphibole, Pl — plagioclase, Qtz — quartz, Ilm — ilmenite, Spn — sphene, and Ap — apatite.

approach on an EPMA-1600 electron probe at the State Key Laboratory of Ore Deposit Geochemistry (SKLODG), Institute of Geochemistry, Chinese Academy of Sciences in Guiyang. Standard operating conditions include 25 kV for accelerating voltage, 10 nA for specimen current and 10 μm for beam diameter. SPI mineral standards (USA) were used for calibration.

4.2. Whole-rock major and trace element analyses

Major elements of whole-rocks were determined on an Axios PW4400 X-ray fluorescence spectrometer (XRF) at the SKLODG, using fused lithium-tetraborate glass pellets. Analytical precision is better than 5%. Trace elements were analyzed using a PE DRC-e ICP-MS at the SKLODG. 50 mg powdered samples were dissolved in high-pressure Teflon bombs using HF and HNO_3 acids mixture at about 190 °C for 2-days, with Rh as an internal standard to monitor signal drift during counting. Detailed analytical methods were introduced by Qi et al. (2000). Analytical precision is better than 10%.

4.3. Whole-rock Sr and Nd isotopic analyses

Whole-rock Sr–Nd isotopic compositions were obtained using a Finnigan Triton multi-collector mass spectrometer at the China University of Geosciences, Wuhan. The mass fractionation corrections for Sr and Nd isotopic ratios are based on $^{86}Sr/^{88}Sr = 0.1194$ and $^{146}Nd/^{144}Nd = 0.7219$, respectively. The $^{87}Sr/^{86}Sr$ ratios of the NBS9 ^{87}Sr standards and $^{143}Nd/^{144}Nd$ ratios of the La Jolla Nd standards determined during this study were 0.710254 ± 0.000008 (n = 18) and 0.511856 ± 0.000012 (n = 15), respectively. Total procedural blanks are Rb = 3×10^{-11}, Sr = 1.2×10^{-10}, Sm = 3×10^{-11}, and Nd = 1.2×10^{-10}. Detailed procedures were given by Zhou et al. (2007).

4.4. Zircon O and Hf isotopic analyses

The samples for zircon O and Hf isotopic analyses were collected from each phase of the Xiuwacu pluton, and from the Relin, Hongshan, and Tongchanggou intrusions. These samples include biotite granitic porphyry (Xiuwacu phase 1, XWC11-32), monzogranite (Xiuwacu phase 2, XWC11-31), alkali–feldspar leucogranite (Xiuwacu phase 3, XWC11-01), monzogranitic porphyry (Relin, RL11-10), granitic porphyry (Hongshan, HS10-03), and biotite granitic porphyry (Tongchanggou, TCG11-01).

Zircon grains were separated using conventional heavy liquid and magnetic separation techniques. Representative zircon grains were hand-picked under a binocular microscope, mounted in an epoxy resin disk, and polished to about half their thickness for analysis. The Zircons were documented with transmitted and reflected light micrographs as well as cathodoluminescence (CL) images to reveal their

internal structures. The CL images were obtained using LEO1450VP scanning electron microscope at the Institute of Geology and Geophysics, Chinese Academy of Sciences (IGG, CAS), Beijing.

Zircon oxygen isotopes were measured by using the Cameca IMS-1280 SIMS at the IGG, CAS in Beijing. Detailed analytical procedures were described by (Li et al., 2009b). The Cs^+ primary ion beam was used as the ion source. Spot size is about 20 μm in diameter. Oxygen isotopes were measured using the multi-collection model on two off-axis Faraday cups. Each analysis takes ~4 min. Uncertainty on individual analysis usually is less than 0.2‰ (1σ) (Li et al., 2010a). The instrumental mass fractionation factor was corrected using zircon Penglai and Qinghu standards with a $\delta^{18}O$ value of 5.31‰ ± 0.10‰ (2 SD) and 5.4‰ ± 0.2‰ (2 SD), respectively (Li et al., 2010b, 2013b). Results of the standard zircons Qinghu and Penglai determined in this study are listed in the Appendix 1.

Zircon Lu–Hf isotopic analyses were conducted using a Neptune Plus MC–ICP-MS (Thermo Fisher Scientific, Germany) equipped with a Geolas 2005 excimer ArF laser ablation system (Lambda Physik, Göttingen, Germany) at the state Key Laboratory of Geological Processes and Mineral Resources, China University of Geosciences in Wuhan. A "wire" signal smoothing device was included in this laser ablation system, by which smooth signals could be produced even at very low laser repetition rates down to 1 Hz (Hu et al., 2012b). The energy density of laser ablation used in this study was 5.3 J cm^{-2}. Helium was used as the carrier gas within the ablation cell and was merged with argon (makeup gas) after the ablation cell. The 193 nm laser a consistent 2-fold signal enhancement was achieved in helium than in argon gas (Hu et al., 2008b). A simple Y junction downstream from the sample cell was used to add small amounts of nitrogen (4 ml min^{-1}) to the argon makeup gas flow (Hu et al., 2008a). All data were acquired on zircon in single spot ablation mode at a spot size of 44 μm in this study. Each measurement consisted of 20 s of acquisition of the background signal followed by 50 s of ablation signal acquisition. Detailed operating conditions for the laser ablation system and the MC–ICP-MS instrument and analytical method are the same as described by Hu et al. (2012a). Our determined $^{176}Hf/^{177}Hf$ ratios of 0.282309 ± 0.000024 (2σ, n = 20) for zircon standard 91500 are well consistent with the reported values $^{176}Hf/^{177}Hf$ ratios of 0.282306 ± 0.000010 (2σ) by Woodhead et al. (2004).

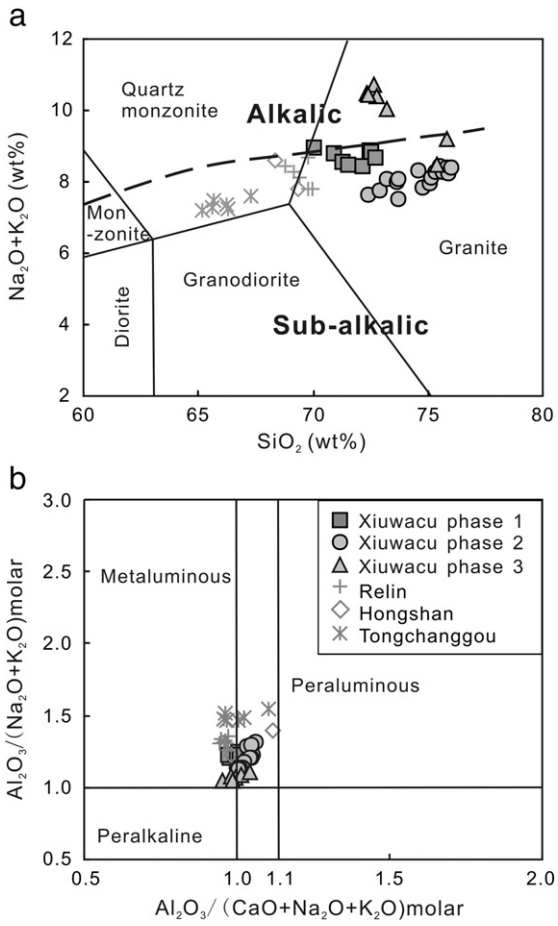

Fig. 4. (a) Total alkali versus SiO_2 diagram (Middlemost, 1994); (b) A/NK versus A/CNK diagram (Maniar and Piccoli, 1989) for Late Cretaceous intrusions in the southern Yidun Terrane.

5. Results

5.1. Mineral chemistry

Plagioclase and biotite are two of the major crystallizing minerals for the four intrusions in the southern Yidun Terrane. Results of their mineral composition analyses are listed in the Appendix 2. Plagioclase in the Tongchanggou, Hongshan, Relin, Xiuwacu phase 1, and MMEs in Xiuwacu phase 1 show similar variations in An values ranging from 21 to 59. The plagioclase phenocrysts have normal oscillatory zoning composition. In addition, the An values of plagioclase in the Xiuwacu pluton decline from Xiuwacu phase 1 (21–59) to phase 2, (15–16) then to phase 3 (4–7) (Appendix 2), conforming to the Bowen's reaction series.

Biotite in the Tongchanggou, Hongshan, Relin, MMEs in Xiuwacu phase 1, Xiuwacu phase 1, and Xiuwacu phase 2 have similar SiO_2 (34.88–37.42 wt.%) and Al_2O_3 (12.01–14.33 wt.%) contents and A/CNK values (1.2–1.5), but have variable FeO (18.82–30.65 wt.%) and MgO (4.81–13.16 wt.%) contents and Mg# values (0.22–0.55). In addition, MgO contents and Mg# values of those earlier mentioned intrusions show good decreasing trends from Tongchanggou to the Xiuwacu phase 2 in order. The Xiuwacu phase 3 has the highest Al_2O_3 (27.27–32.20 wt.%), SiO_2 (45.36–50.37 wt.%), and K_2O (9.95–10.55 wt.%) contents and A/CNK values (2.5–2.9), but has lowest FeO (2.09–3.13 wt.%) and MgO (2.38–5.33 wt.%) values (Appendix 2). Generally, the variation of the composition of plagioclase and biotite in these intrusions probably indicates the fractional crystallization process.

5.2. Major and trace elements

Major and trace elemental data from the three phases of the Xiuwacu pluton are listed in Appendix 3. SiO_2 contents in the phase 1 biotite granitic porphyry (70.0–72.7 wt.%) are relatively lower than those in the phase 2 monzogranite (72.4–76.0 wt.%) and in the phase 3 alkali–feldspar leucogranite (72.7–75.4 wt.%). In the total alkali–silica (TAS) diagram, all samples from the three phases fall into the field of granite with phase 1 and 2 being sub-alkalic but phase 3 being alkalic (Fig. 4a). They are metaluminous and slightly peraluminous granites (A/CNK = 0.96–1.07) (Fig. 4b). Generally, the contents of $Fe_2O_3^T$, MgO, CaO, P_2O_5, TiO_2, and MnO gradually decrease from phase 1 through phase 2 to phase 3 (Fig. 5). However, phase 3 shows the highest Al_2O_3, Na_2O, K_2O, and $Na_2O + K_2O$ contents, K_2O/Na_2O ratio, and aluminum saturation index [ASI = molar $Al_2O_3/(CaO + Na_2O + K_2O - 0.67P_2O_5)$] (Frost et al., 2001), whereas phase 2 has the lowest (Fig. 5). In the Harker diagrams of selected major oxides and trace elements, Al_2O_3, $Fe_2O_3^T$, MgO, CaO, P_2O_5, TiO_2, and Sr of phase 1 and phase 2 correlate negatively with SiO_2 (Fig. 5).

In the chondrite-normalized rare earth element (REE) diagrams, the samples from phases 1 and 2 display highly fractionated REE patterns with La/Yb ratios of 6–32 and moderately negative Eu anomalies ($Eu/Eu^* = 0.24–0.59$) (Fig. 6). In the primitive mantle-normalized trace element diagram, all the samples are depleted in Ba, Nb, Sr, P, and Ti, and are enriched in Rb, Th, U, and Ta (Fig. 6). In contrast, the

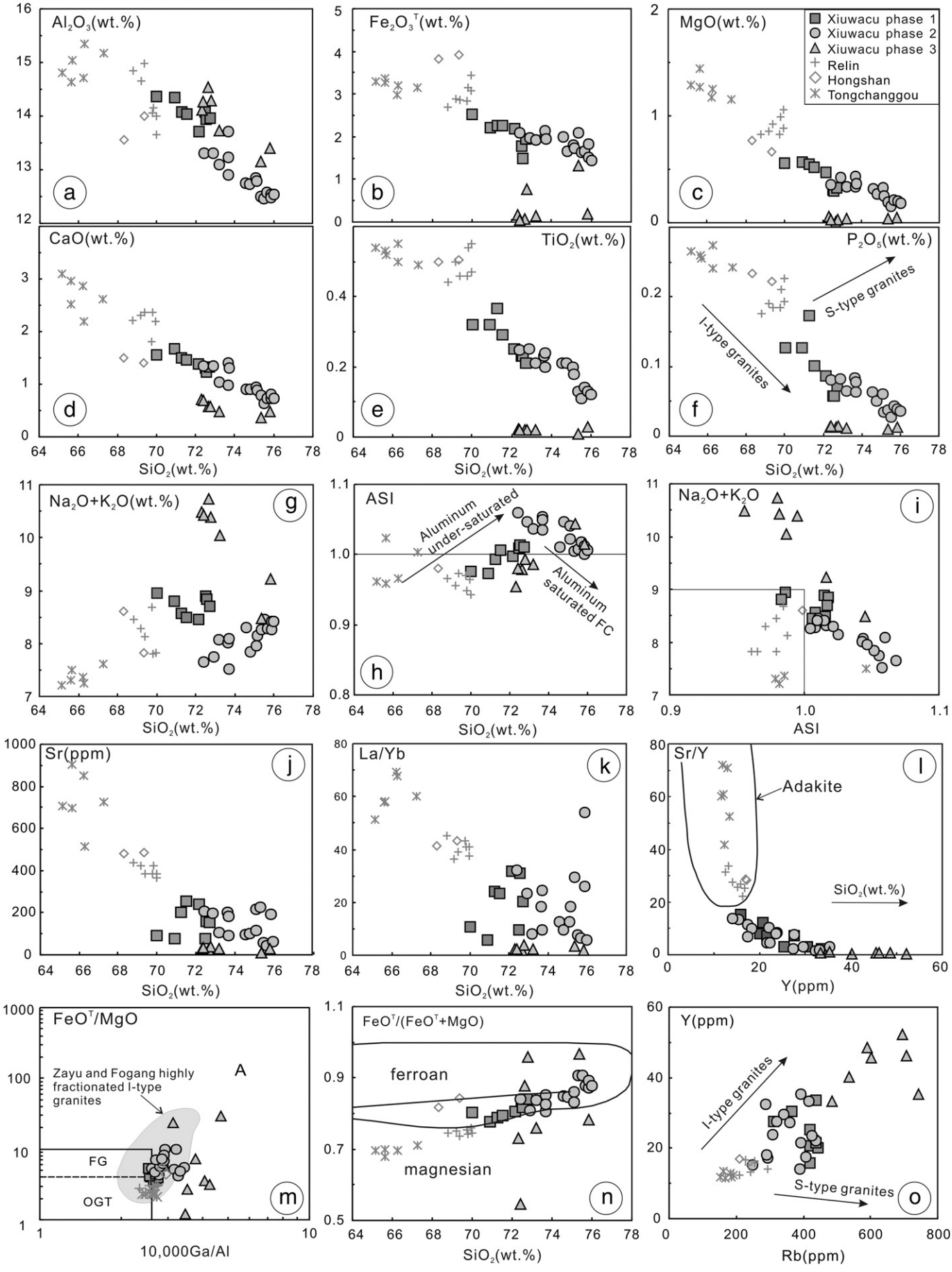
Al2O3(wt.%)
a
Fe2O3T(wt.%)
b
MgO(wt.%)
c
Xiuwacu phase 1
Xiuwacu phase 2
Xiuwacu phase 3
Relin
Hongshan
Tongchanggou
CaO(wt.%)
d
TiO2(wt.%)
e
P2O5(wt.%)
S-type granites
I-type granites
f
SiO2(wt.%)
Na2O+K2O(wt.%)
g
ASI
Aluminum under-saturated
Aluminum saturated FC
h
Na2O+K2O
i
ASI
Sr(ppm)
j
La/Yb
k
Sr/Y
Adakite
SiO2(wt.%)
l
Y(ppm)
FeOT/MgO
Zayu and Fogang highly fractionated I-type granites
A
FG
OGT
m
10,000Ga/Al
FeOT/(FeOT+MgO)
ferroan
magnesian
n
Y(ppm)
I-type granites
S-type granites
o
Rb(ppm)

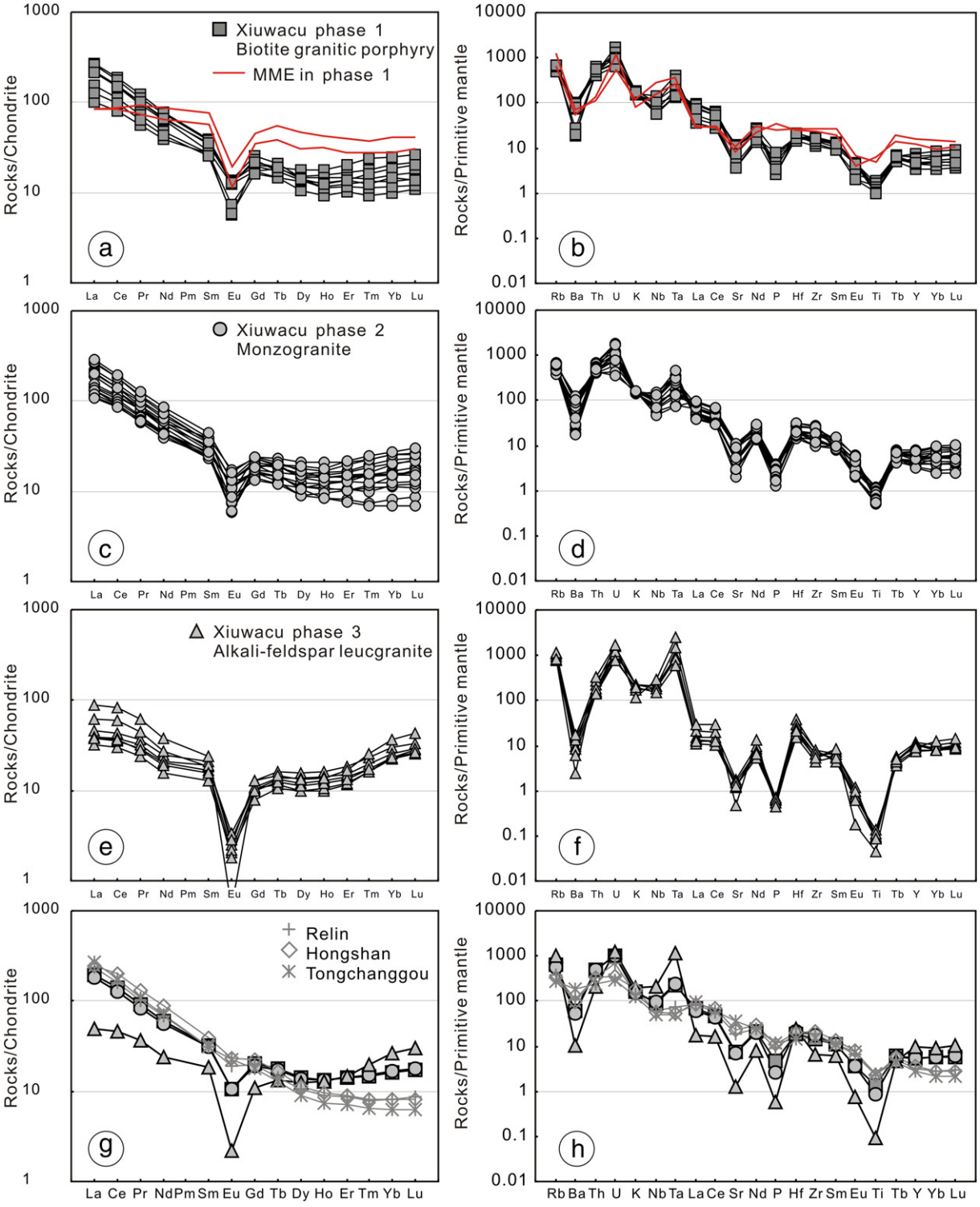

Fig. 6. Chondrite-normalized rare earth elements (REE) and primitive mantle-normalized trace element diagrams for the intrusions in the southern Yidun Terrane. Chondrite normalizing values and primitive mantle values are from Sun and McDonough (1989). Data for the Relin, Hongshan and Tongchanggou intrusions are from Wang et al. (2014).

phase 3 samples show less fractionated light REE (LREE)/heavy REE (HREE) with lower La/Yb ratios (2.0–3.8) and intense Eu anomalies (Eu/Eu* = 0.14–0.23). Phase 3 is also heavily depleted in Ba, Sr, P, and Ti, and is enriched in Rb, Th, U, and Ta.

5.3. Whole-rock Sr and Nd isotopes

Sr and Nd isotopic compositions of the three phases of the Xiuwacu pluton, and of Relin, Hongshan, and Tongchanggou

Fig. 5 Chemical variation diagrams for the Late Cretaceous intrusions in the southern Yidun Terrane.Data for the Relin, Hongshan, and Tongchanggou intrusions are from Wang et al. (2014). The trends of I-type and S-type granites in figures (f) and (O) are from Li et al. (2007). The adakite field in the figure (l) is after Richards and Kerrich (2007). The figures (l) and (m) are after Whalen et al. (1987), FG = Fractionated M-, I- and S-type granites, OGT = unfractionated M-, I- and S-type granites; Zayu and Fogang highly fractionated I-type granites are from Zhu et al. (2009b) and Li et al. (2007), respectively. The figure (n) is after Frost et al. (2001).

Table 2
Sr–Nd isotope analyses of Late Cretaceous intrusions in the Southern Yidun Terrane.

Sample. nos.	Petrology	Rb	Sr	$^{87}Rb/^{86}Sr$	$^{87}Sr/^{86}Sr$	±2σ	$(^{87}Sr/^{86}Sr)t$	Sm	Nd	$^{147}Sm/^{144}Nd$	$^{143}Nd/^{144}Nd$	±2σ	$(^{143}Nd/^{144}Nd)t$	εNd(t)	T_{DM2}
XWC11-32	Biotite granitic porphyry	366	90.6	11.719	0.721695	4	0.7075	4.13	22.14	0.1127	0.512237	3	0.51217	−6.9	1450
XWC11-33	Biotite granitic porphyry	312	204	4.425	0.713422	5	0.7081	5.94	36.54	0.0982	0.512205	5	0.51215	−7.4	1488
SXWC10-29	Monzogranite	295	198	4.312	0.712908	5	0.7077	4.25	26.2	0.0980	0.512205	7	0.51215	−7.4	1488
SXWC10-04	Monzogranite	434	101	12.449	0.722964	4	0.7079	3.54	20.7	0.1033	0.512205	4	0.51215	−7.4	1493
SXWC10-07	Monzogranite	394	107	10.666	0.721374	4	0.7085	5.91	27.2	0.1313	0.512210	5	0.51214	−7.6	1509
XWC10-14	Monzogranite	291	184	4.578	0.713064	4	0.7075	4.67	27.8	0.1015	0.512215	5	0.51216	−7.2	1475
SXWC10-45	Alkali–feldspar leucogranite	360	57.9	18.025	0.729223	4	0.7075	3.77	18.4	0.1238	0.512220	6	0.51215	−7.4	1487
XWC11-01	Alkali–feldspar leucogranite	695	25.5	79.546	0.804946	5	0.7089	3.91	11.64	0.2029	0.512231	3	0.51212	−8.0	1539
SXWC10-18	Alkali–feldspar leucogranite	537	10.1	156.688	0.899085	7	0.7098	3.67	17.6	0.1260	0.512210	4	0.51214	−7.6	1505
XWC11-26	MME	405	229	5.119	0.714106	6	0.7079	11.70	40.31	0.2585	0.512252	4	0.51211	−8.2	1579
XWC11-27	MME	770	169	13.203	0.725156	18	0.7092	8.67	30.37	0.2631	0.512241	4	0.51209	−8.5	1600
RL12-01	Monzogranite	293	386	2.196	0.710371	8	0.7078	4.77	30.90	0.1460	0.512227	4	0.51215	−7.5	1488
RL12-08	Monzogranite	254	425	1.729	0.709790	8	0.7078	4.95	31.50	0.1489	0.512219	2	0.51214	−7.7	1502
HS12-05	Granitic porphyry	209	483	1.252	0.709670	6	0.7082	5.97	41.20	0.1375	0.512197	2	0.51212	−8.0	1530
TCG12-05	Biotite granitic porphyry	152	726	0.606	0.707640	6	0.7069	4.31	30.10	0.1360	0.512333	10	0.51226	−5.3	1315
TCG12-10	Biotite granitic porphyry	182	905	0.582	0.707624	6	0.7069	5.11	33.70	0.1442	0.512323	4	0.51225	−5.6	1337

Note: all the initial isotopic ratios were corrected to 85 Ma. Rb, Sr, Sm and Nd abundances for the samples were determined by ICP-MS. $\varepsilon_{Nd}(t)$ values are calculated using present-day $(^{147}Sm/^{144}Nd)_{CHUR} = 0.1967$ and $(^{143}Nd/^{144}Nd)_{CHUR} = 0.512638$. T_{DM} values are calculated using present-day $(^{147}Sm/^{144}Nd)_{DM} = 0.2137$ and $(^{143}Nd/^{144}Nd)_{DM} = 0.51315$. The details for two-stage (T_{DM2}) Nd model age calculations are given by Wu et al. (2002). Two-stage Nd model age (T_{DM2}) is calculated using the same formulation as Keto and Jacobsen (1987).

intrusions are shown in Table 2. The phase 1 samples (two samples) display homogeneous $(^{87}Sr/^{86}Sr)_i$ (0.7075–0.7081) and $\varepsilon_{Nd}(t)$ (−7.4 to −6.9) values with T_{DM2} = 1.49–1.51 Ga. The phase 2 samples (four samples) have similar $(^{87}Sr/^{86}Sr)_i$ = 0.7075–0.7085 and $\varepsilon_{Nd}(t)$ = −7.6 to −7.2 values with T_{DM2} = 1.49–1.51 Ga. The phase 3 (three samples) display $(^{87}Sr/^{86}Sr)_i$ = 0.7075–0.7098 and $\varepsilon_{Nd}(t)$ = −8.0 to −7.4 values with T_{DM2} = 1.49–1.51 Ga. The MMEs from Xiuwacu intrusions (two samples) have $(^{87}Sr/^{86}Sr)_i$ (0.7079–0.7092) and $\varepsilon_{Nd}(t)$ (−8.5 to −8.2) values with T_{DM2} = 1.58–1.60 Ga. The Relin and Hongshan intrusions (three samples)

Fig. 7. CL images of representative zircons analyzed for in situ Hf and O isotopes. Small ellipses indicate the SIMS analyzing spots for O isotopes, and the big circles denote the LA–MC–ICPMS analyzing spots for Hf isotopes. Numbers near the analyzing spots are the spots' no. and $\delta^{18}O/\varepsilon_{Hf}(t)$ values.

have similar $(^{87}Sr/^{86}Sr)_i = 0.7078–0.7082$ and $\varepsilon_{Nd}(t) = -8.0$ to -7.5 values with $T_{DM2} = 1.49–1.53$ Ga. The Tongchanggou (two samples) display $(^{87}Sr/^{86}Sr)_i = 0.7075–0.7098$ and $\varepsilon_{Nd}(t) = -5.6$ to -5.3 values with $T_{DM2} = 1.32–1.38$ Ga.

5.4. Zircon O and Hf isotopes

Most zircons from the samples in the Shangri-La region are colorless, euhedral, and have igneous oscillatory zoning. Lengths of the zircon

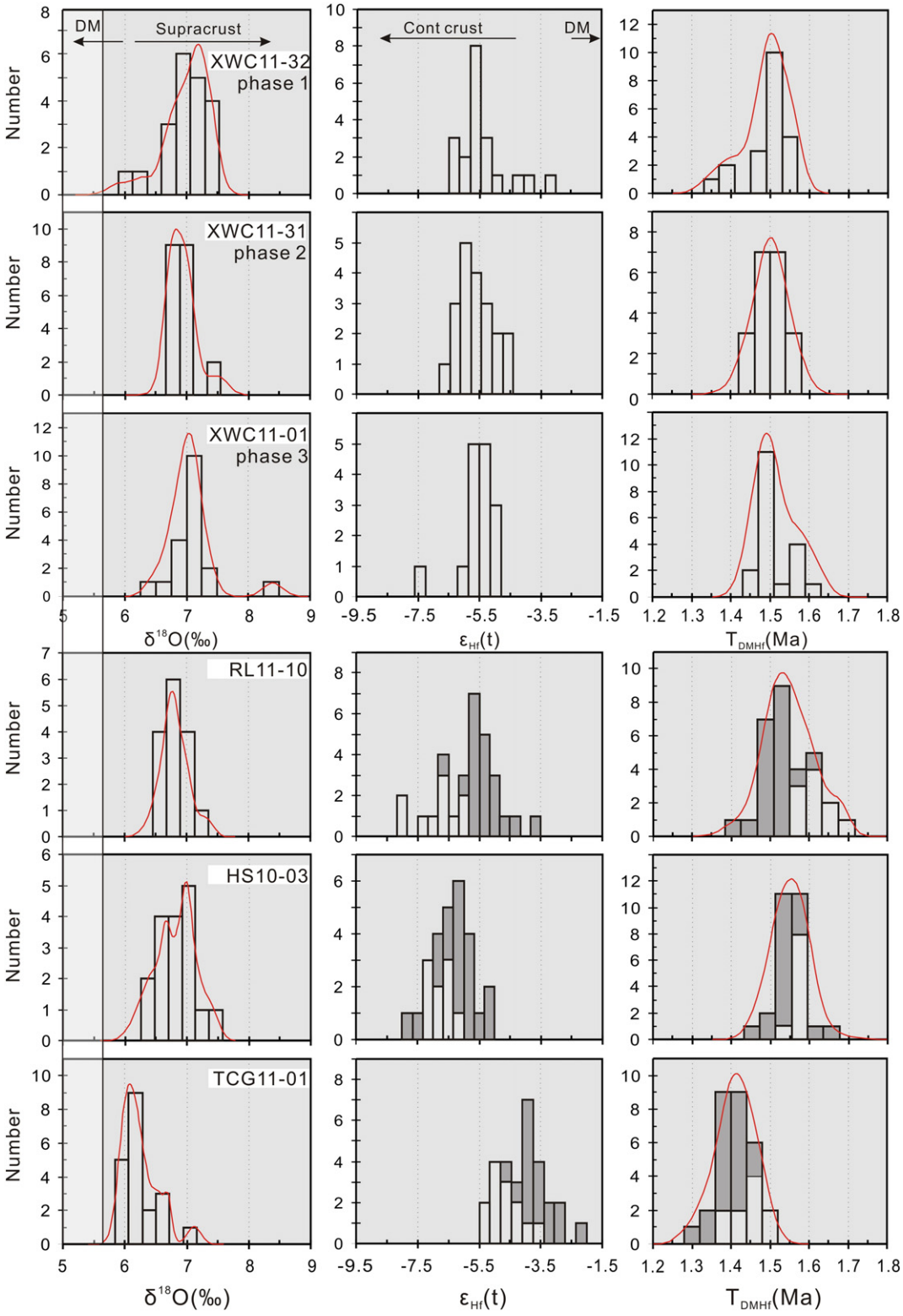

Fig. 8. Histogram of $\delta^{18}O$ and $\varepsilon_{Hf}(t)$ values and Hf model ages for the intrusions in the southern Yidun Terrane. Dark gray column represent $\varepsilon_{Hf}(t)$ values and Hf model ages from Wang et al. (2014).

grains mainly vary from 60 μm to 300 μm, with length to width ratios from ~2:1 to 3:1. The representative cathodoluminescence (CL) images of the zircons are shown in Fig. 7.

5.4.1. Zircon O and Hf isotopes of the Xiuwacu pluton

Fifty-nine in situ O and Hf isotopic analyses were conducted on zircons from the three phases in the Xiuwacu area. The data are given in Appendix 1 and Appendix 4. Zircons from the phase 1 biotite granitic porphyry, show $\delta^{18}O$ values ranging from 5.9‰ to 7.4‰ with a weighted mean value of 7.0 ± 0.1‰ (2σ). Zircons from the phase 2 monzogranite present relatively homogenous $\delta^{18}O$ values ranging from 6.7‰ to 7.5‰ with a weighted mean value of 6.9 ± 0.1‰ (2σ). Zircons from the phase 3 alkali–feldspar leucogranite display a wider range of $\delta^{18}O$ values from 6.4‰ to 8.4‰ with a weighted mean value of 7.1 ± 0.2‰ (2σ) (Fig. 8).

Lu–Hf isotopic analyses were conducted on the same zircons grains that for the O isotopic analyses. The zircon $\varepsilon_{Hf}(t)$ values from the phase 1, 2, and 3 intrusions were back-calculated to 85.5 Ma, 84.8 Ma, and 84.4 Ma, respectively. Twenty analyses on the phase 1 zircons yielded $\varepsilon_{Hf}(t)$ values between −6.5 and −3.2 with T_{DM2} model ages of 1.35 to 1.56 Ga. Twenty analyses on the phase 2 zircons yielded $\varepsilon_{Hf}(t)$ values between −6.6 and −4.4 with T_{DM2} model ages of 1.43 to 1.57 Ga. Fifteen analyses on the phase 3 zircons yielded $\varepsilon_{Hf}(t)$ values between −7.6 and −4.8 with T_{DM2} model ages of 1.45 to 1.63 Ga (Fig. 8).

5.4.2. Zircon O and Hf isotopes of Relin, Hongshan, and Tongchanggou intrusions

Fifty-three in situ O isotopic analyses were conducted on zircons from the 82.7 Ma Relin, 81.1 Ma Hongshan, and 86.7 Ma Tongchanggou intrusions. The data are given in Appendix 1 and Appendix 4. Zircons from the Relin intrusion present relatively homogenous $\delta^{18}O$ values ranging from 6.5‰ to 7.3‰ with a weighted mean value of 6.8 ± 0.1‰ (2σ). Likely, zircons from the Hongshan intrusion show $\delta^{18}O$ values between 6.3‰ and 7.4‰ with a weighted mean value of 6.9 ± 0.1‰ (2σ). Zircons from the Tongchanggou intrusion also display homogenous $\delta^{18}O$ values of 5.9–7.1‰ but with a lower weighted mean value of 6.3 ± 0.2‰ (2σ) (Fig. 8).

Lu–Hf isotopic analyses were conducted on the same zircon grains. Ten analyses for Relin yielded $\varepsilon_{Hf}(t)$ values between −6.5 and −8.6 with T_{DM2} model ages of 1.56 to 1.69 Ga. Nine analyses for Hongshan yielded $\varepsilon_{Hf}(t)$ values between −7.1 and −6.1 with T_{DM2} model ages of 1.53 to 1.59 Ga. Nineteen analyses for Tongchanggou yielded $\varepsilon_{Hf}(t)$ values between −5.3 and −3.9 with T_{DM2} model ages of 1.40 to 1.48 Ga (Fig. 8).

6. Discussion

6.1. Geochemical affinities of the Xiuwacu pluton

Previous studies have suggested that the Xiuwacu intrusions are A-type granites (Hou and Zhou, 2001; Zeng et al., 2003). In this study, all rock samples from the three phases of the Xiuwacu pluton have high SiO_2 (70–76 wt.%), $Na_2O + K_2O$ (7.5–10.7 wt.%), 10,000 Ga/Al (2.5–4.7), Nb (32.6–212.0 ppm) and Zr (48.8–302 ppm), and low CaO (0.39–1.67 wt.%), MgO (0.01–0.57 wt.%) and Sr (10.1–256 ppm) values (Appendix 3). However, these values show a wide range of variation, which indicates that those magmas are not as homogeneous as the classical A-type granites (Collins et al., 1982; Eby, 1990; Whalen et al., 1987). There are clear decreasing trends in contents of $Fe_2O_3^T$, CaO, MgO, TiO_2, Sr, and Ba with an increasing SiO_2 trend from the phase 1 to phase 2, and to phase 3 (Fig. 5). The samples show good trends of fractional crystallization. The majority of these samples have relatively low FeO^T/MgO ratios (<10) and Zr + Nb + Ce + Y values (<350 ppm) and fall within the field of high fractional crystallization felsic granites in the 10,000 * Ga/Al versus FeO^T/MgO diagrams (Fig. 5m; Appendix 3; Li et al., 2007; Whalen et al., 1987; Zhu et al., 2009b). Furthermore, paired with the intensive fractionation, the $FeO^T/(FeO^T + MgO)$ ratios also show a positive correlation with SiO_2 (Fig. 5n). All these geochemical features suggest that the Xiuwacu pluton is composed of high fractional crystallization granites rather than A-type granites. Noticeably the A/CNK values of all rocks from the Xiuwacu pluton are lower than 1.1, which is distinguishable from the highly felsic S-type granites that commonly are strongly peraluminous with A/CNK values much higher than 1.1 (Fig. 4b; Chappell and White, 2001; Sylvester, 1998). Peraluminous minerals such as muscovite, cordierite, garnet, and Al_2SiO_5 polymorph, as diagnostic minerals in S-type granites (Barbarin, 1999), are rarely founded in the phase 1 and phase 2 intrusions. In addition, the P_2O_5 content of those rocks decrease markedly at higher SiO_2, thereby showing good trends of I-type granites (Fig. 5f; Chappell and White, 1992; Li et al., 2007). The Y content correlate positively with the Rb in those rocks, which also shows a typical I-type granite evolution trend (Fig. 5o; Li et al., 2007). In sum, our new evidences suggest that the three phases of the Xiuwacu pluton are highly fractionated I-type granites rather than A-type granites or S-type granites.

6.2. Fractional crystallization

As mentioned above, the Xiuwacu, Relin, Hongshan, and Tongchanggou intrusions are contemporaneous I-type granites formed

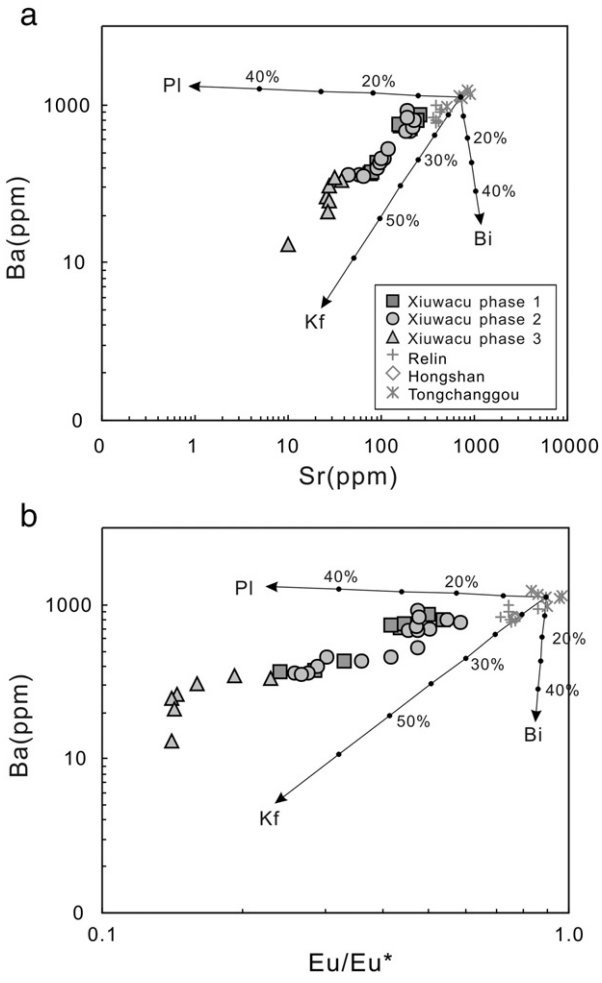

Fig. 9. (a) Ba versus Sr and (b) Ba versus Eu/Eu* plots for the Late Cretaceous intrusions in the southern Yidun Terrane. Vectors for plagioclase (Pl), K-feldspar (Kf) and biotite (Bi) fractionation are calculated using partition coefficients of Ewart and Griffin (1994). The composition of the biotite granitic porphyry sample from Tongchanggou intrusion (TCG12-13) (Wang et al., 2014) is assumed to be parental magma. Tick marks indicate percentage of mineral phase removed, in 10% intervals.
Data for the Relin, Hongshan and Tongchanggou intrusions are from Wang et al. (2014).

around 85 Ma (Wang et al., 2014). In the Harker diagram, Al_2O_3, $Fe_2O_3^T$, MgO, CaO, TiO_2, P_2O_5, and Sr values, and Sr/Y and La/Yb ratios correlate negatively with SiO_2 (Fig. 5a–f and j–l). Combing with the variation in the composition of plagioclase and biotite in those intrusions (Appendix 2), it indicates a good fractional crystallization sequence for Tongchanggou, Hongshan, Relin, Xiuwacu phase 1, Xiuwacu phase 2, and Xiuwacu phase 3. Mafic minerals (i.e., amphibole, clinopyroxene, and biotite), Fe–Ti oxides, feldspars, and apatite were probably involved during the fractionation process (Zhong et al., 2009; Zhu et al., 2011b). Separation of mafic minerals resulted in low contents of $Fe_2O_3^T$ (0.04–2.52%) and MgO (0.01–0.57%). Depletion in Nb, Ti, and P is considered to be associated with fractionation of Ti-bearing phases such as ilmenite and titanite, and apatite. Low CaO (0.37–1.67%) contents and moderately to strongly negative anomalies of Ba, Sr, and Eu indicate an extensive fractionation of plagioclase and/or K-feldspar (Wu et al., 2003a). In the Ba versus Sr and Ba versus Eu/Eu* diagrams, all the samples mainly distribute between the vectors of plagioclase and K-feldspar (Fig. 9), which probably indicates that both plagioclase and K-feldspar were fractional mineral during the fractionation process. A decreasing An trend of plagioclase from the Xiuwacu phase 1 to phase 3 (Appendix 2) also indicates the separation of plagioclase. During the early stage of magmatic evolution, the $Na_2O + K_2O$ contents and ASI values increased with SiO_2 when aluminum was unsaturated (Fig. 5g–i). Then, as those rock properties changed from metaluminous to weakly peraluminous ($1.0 < ASI < 1.1$), aluminous biotite were separated from magmas reducing the ASI values (Appendix 2; Frost et al., 2001). Thus, K-feldspar, plagioclase and aluminous biotite were probably fractionated during the evolution process.

6.3. Magma source

The I-type Tongchanggou, Relin, and Hongshan granites, and the three phases of the Xiuwacu pluton in the southern Yidun Terrane have similar whole-rock Sr–Nd and zircon Hf–O isotopic compositions (Figs. 10 and 11), which indicates similar origins. In general, intermediate to felsic I-type granites have been proposed to have formed via several mechanisms: (1) advanced fractional crystallization of mantle-derived parental magmas, with or without crustal assimilation (Chiaradia, 2009; Li et al., 2009a); (2) mixing of the melts from partial melting of supracrustal sedimentary rocks and mantle-derived magmas (Kemp et al., 2007; Li et al., 2009b; Zhu et al., 2009b); and (3) remelting of preexisting infracrustal igneous rocks, with or without mantle-derived magma input (Chappell and White, 2001; Griffin et al., 2002; Wu et al., 2003b; Yang et al., 2004).

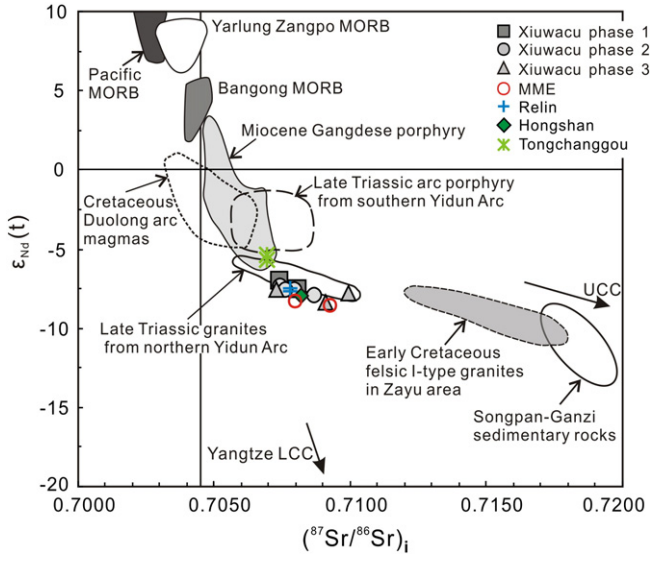

Fig. 10. $\varepsilon_{Nd}(t)$ and $(^{87}Sr/^{86}Sr)_i$ diagram of the intrusions in the southern Yidun Terrane. The initial isotopic ratios of these intrusions are from Table 2.
The trends of the lower continental crust (LCC) are from Jahn et al. (1999). Pacific MORB are from Hofmann (2003); Yarlung–Zangbo MORB from Xu and Castillo (2004); Bangong MORB from Bao et al. (2007); Cretaceous Duolong arc magmas from Li et al. (2013a); Miocene Gangdese porphyry from Hou et al. (2013); Late Triassic arc magmas in the southern Yidun Terrane from (Leng et al. (2012); Wang et al. (2011a)); Late Triassic granites in the northern Yidun Terrane from He et al. (2013); Early Cretaceous felsic I-type granites in Zayu area from Zhu et al. (2009b); Songpan–Ganzi sedimentary rocks from Wu et al. (2010).

The Xiuwacu, Relin, Hongshan, and Tongchanggou intrusions have high SiO_2 contents (63–76 wt.%) and zircon $\delta^{18}O$ (5.9‰ to 8.4‰) values contrasting to the magmas that derived from direct partial melting of the mantle, as the latter have low $\delta^{18}O$ (5.3 ± 0.3‰, 1σ) values and cannot yield melts more silicic than andesitic compositions (Baker et al., 1995; Green, 1973; Valley et al., 2005). The magmas, predominately derived from fractional crystallization of mantle-derived parental magmas, have low $\delta^{18}O$ values (<6.5‰) (Valley et al., 2005); however, the four intrusions in the southern Yidun Terrane have relatively higher zircon $\delta^{18}O$ values mostly ranging from 6.5‰ to 7.5‰. In addition, the four intrusions are much more enriched in crustal material comparing to other Mesozoic magmas such as Bangong mid-ocean ridge basalt (MORB) (Bao et al., 2007), Early Cretaceous Duolong arc magmas (Li et al., 2013a), and Late Triassic arc magmas in the southern Yidun Terrane (Leng et al., 2012; Wang et al., 2011a). All these magmas were formed by assimilation fractional crystallization (AFC) of mantle-derived magmas (Fig. 10). Thus, the four intrusions in the southern Yidun Terrane probably could not have been generated by high fractionation crystallization of basaltic magmas; their relatively high $(^{87}Sr/^{86}Sr)_i$ (0.7075–0.7098), and negative $\varepsilon_{Hf}(t)$ (−8.6 to −3.2) and $\varepsilon_{Nd}(t)$ (−8.0 to −6.9) values (Table 2; Figs. 10 and 11), and ancient Hf and Nd model ages (1.7–1.3 Ga) (Fig. 8) probably indicate a dominant crustal source.

All the rocks from the Xiuwacu, Relin, Hongshan, and Tongchanggou intrusions are metaluminous or slightly peraluminous granites (A/CNK = 0.96–1.07), low P_2O_5, and are different from the magmas derived from partial melting of the supracrustal sedimentary rocks (Chappell and White, 2001). Their $(^{87}Sr/^{86}Sr)_i$ (0.7075–0.7098) and $\delta^{18}O$ (5.9‰ to 8.4‰) values are markedly lower than the supracrustal sediments from the Songpan–Ganzi Fold Belt [$(^{87}Sr/^{86}Sr)_i$ = 0.7173–0.7196] (Wu et al., 2010) and the S-type granites ($\delta^{18}O$ = 8.4–11.3‰) (Li et al., 2009b) from South China (Figs. 10 and 11). In addition, their $(^{87}Sr/^{86}Sr)_i$, $\varepsilon_{Hf}(t)$, and $\delta^{18}O$ values between the supracrustal sediments end-member and mantle end-member are less variable than those of the high fractional I-type Fogang granites [$\varepsilon_{Hf}(t)$ = −10.3 to −3.1 and $\delta^{18}O$ = 5.6‰ to 9.0‰; Fig. 11; Li et al., 2007; Li et al., 2009b] and the Jindabyne and Why Worry I-type granitic suite [$\varepsilon_{Hf}(t)$ = −8.4 to −0.8 and $\delta^{18}O$ = 4.8‰ to 9.3‰; Fig. 11; Kemp et al., 2007], which indicates that the four intrusions may not be formed by the mingling of melts derived from partial melting of supracrustal sedimentary rocks and mantle-derived magmas.

In contrast, their $(^{87}Sr/^{86}Sr)_i$ (0.7075–0.7098) and $\delta^{18}O$ (5.9‰ to 8.4‰) values are more similar to the average values of the lower crust [$(^{87}Sr/^{86}Sr)_i$ = 0.7010 (values of the Yangtze Craton; Jahn et al., 1999) and $\delta^{18}O$ = 7.0‰ (global values; Kempton and Harmon, 1992)], probably indicating that the four intrusions were derived predominantly from partial melting of the lower continental crust. Negative $\varepsilon_{Hf}(t)$ values (−8.6 to −3.2) and ancient Nd and Hf mantle model ages (1.7–1.3 Ga) of the four intrusions are in contrast to the magmas that derived from partial melting of the juvenile lower crust and characterized by positive $\varepsilon_{Hf}(t)$ values and relatively young Nd and Hf mantle model ages (<1.0 Ga) (Hou et al., 2013). This indicates that they were mainly derived from ancient continental crustal sources. As mentioned earlier, the Yidun Terrane shares a common crystalline basement with the Yangtze Craton, which in general is isotopically proxied by the Kongling amphibolite in the northern Yangtze Craton (Gao et al., 1999). The ε_{Nd}(85 Ma) (−8.0 to −6.9) values of the four intrusions are much higher than the ancient metasediments [ε_{Nd}(85 Ma) = −37 to −24] and TTG [ε_{Nd}(85 Ma) = −48.7 to −35.6], but more similar

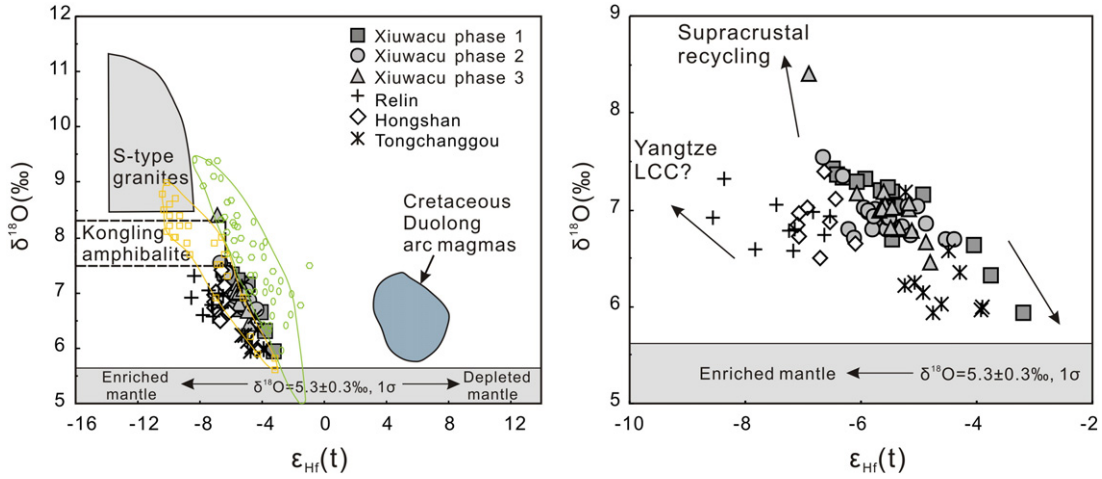

Fig. 11. $\delta^{18}O$ versus $\varepsilon_{Hf}(t)$ diagrams for the intrusions in the southern Yidun Terrane. The field of S-type granites are from Li et al. (2009b); depleted mantle from Valley et al. (2005); Kongling amphibolites are calculated from Zhang et al. (2006); Cretaceous Duolong arc magmas from Li et al. (2013a). Garnet-bearing amphibolite KH35 (Gao et al., 1999) is used to present the Kongling amphibolite. Its mineral composition and oxygen value is as follows: hornblende ca. 54% ($\delta^{18}O = 7.64‰$), plagioclase 43% ($\delta^{18}O = 8.28‰$), garnet 2% ($\delta^{18}O = 8.35‰$) and a few opaques (Zhang et al., 2006). Thus, we evaluated the whole-rock oxygen values of the Kongling amphibolite as $\delta^{18}O = 7.6 \sim 8.3‰$. The green ellipse and hexagon represent the samples from the Jindabyne and Why Worry I-type granitic suite in the Lachlan Fold Belt (Kemp et al., 2007); the yellow unfilled square represent the samples from the Fogang granites in the South China (Li et al., 2009b).

to the amphibolites [$\varepsilon_{Nd}(85\ Ma) = -17.7$ to 0] of the Yangtze Craton in the Kongling region (Gao et al., 1999; Ma et al., 2000). This indicates that these magmas were mainly derived from ancient mafic-intermediate lower crustal sources. In addition, the Relin, Hongshan, and Tongchanggou intrusions have high Sr (363–905 ppm) contents and Sr/Y (22–72) and La/Yb (37–69) ratios, and low MgO (0.66–1.64 wt.%), Y (11.6–17.0 ppm), and HREE (Yb = 0.97–1.59 ppm) contents (Figs. 5 and 6), which has been suggested that they were derived from partial melting of garnet amphibolite with garnet as a residual mineral (Wang et al., 2014).

However, some zircons from the Tongchanggou and Xiuwacu intrusions have lower $\delta^{18}O$ (5.9‰ to 6.3‰) values than the average values of the global lower crust (~7.0‰) (Kempton and Harmon, 1992) and Kongling amphibolite (7.6–8.3‰; Fig. 11a; Zhang et al., 2006), and even lower than the $\delta^{18}O$ values (6.7 ± 0.6%) of lower crustal mafic granulite xenoliths with high Mg numbers (Mg# >70) (Kempton and Harmon, 1992). Those zircons with $\delta^{18}O$ less than 6.5‰ are generally considered to be from formed melts containing a minor to negligible supracrustal component (Kemp et al., 2007; Valley et al., 2005). Combined with their relatively high zircon saturation temperature (mostly ranging from 800 °C to 880 °C; Appendix 3), mantle derived melts were probably evolved to provide heat and mass input to their sources. Furthermore, negative correlations between Hf and O isotopic ratios probably indicate mixing between the ancient mafic-intermediate lower crustal materials and mantle-derived magmas, as Hf and O isotope ratios of the melts parental to zircons are not modified by partial melting in a homogeneous closed system (Kemp et al., 2007; Li et al., 2009b). Moreover, the MMEs with lower SiO_2 (51.9–57.2 wt.%) and higher $Fe_2O_3^T$ and MgO values comparing to the host granitoids widely occurred in the Xiuwacu area (Appendix 3). The enclaves have crenulate and/or chilled margins and have similar trace elemental and whole-rock Sr–Nd isotopic features to the host granitoids (Figs. 6 and 10; Appendix 2; Table 2). Their igneous microtextures are characterized by oscillatory zoning of crystals, euhedral grain shapes, poikilitic biotite and hornblende in quartz and K-feldspar, which is indicative of crystallization of the enclaves from a melt (Keay et al., 1997). In addition, the enclaves have mantled K-feldspar megacrysts with round edges, and typical ocellar texture with spheric shape, corrosion embayments, and hornblende and biotite mantle (Fig. 3h and i) (Barbarin, 2005; Barbarin and Didier, 1992). These field and textural relations also provide striking evidence of in situ microgranular enclave formation by magma mingling (Barbarin and Didier, 1992; Keay et al., 1997).

Fractional crystallization in a closed system from a common parent will produce constant zircon $\delta^{18}O$ values from mafic to felsic melt, whereas open-system assimilation of supracrustal material will yield enriched zircon $\delta^{18}O$ values with increased SiO_2 (Lu et al., 2013; Valley et al., 2005). In the average zircon $\delta^{18}O$ versus SiO_2 diagram (Fig. 12), the average zircon $\delta^{18}O$ values are almost invariable with the increasing SiO_2 trend, which indicates that there was little assimilation of supracrustal sedimentary rocks during the fractional crystallization process though angular fragments of the sandstone from the stratum rocks are found in the final alkali–feldspar leucogranite. Fractional crystallization probably is the main reason for the chemical compositional variations in the Tongchanggou, Relin, and Hongshan intrusions and the three phases of the Xiuwacu intrusion after the mixing between the lower crust- and mantle-derived melts.

In Rb/30 versus Hf versus Ta × 3 tectonic discrimination diagrams (Fig. 13; Harris et al., 1986), the Xiuwacu Late Cretaceous intrusions and other three Late Cretaceous intrusions in the southern Yidun Terrane are plotted in the field of late- or post-collision granites. This indicates that these magmas were formed under a late- or post-collisional extension environment. Therefore, we propose a likely genesis model for these Late Cretaceous magmas in the southern Yidun Terrane:

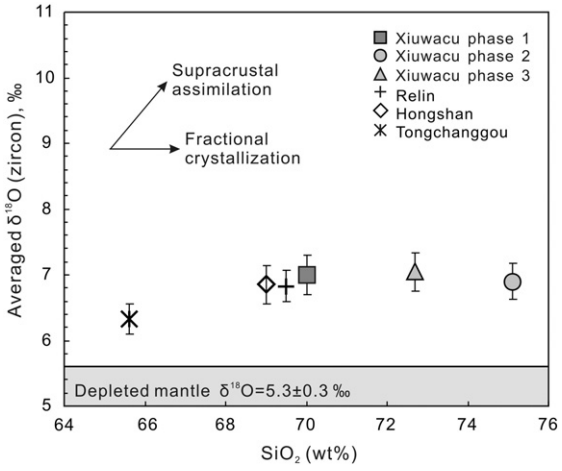

Fig. 12. Whole-rock SiO_2 (wt.%) versus averaged Late Cretaceous magmatic zircon $\delta^{18}O$ values. Supracrustal assimilation and fractional crystallization vectors are shown as arrows.

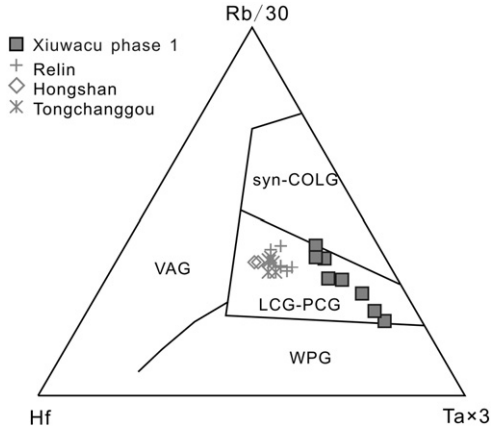

Fig. 13. Rb/30 versus Hf versus Ta × 3 discrimination diagram for the intrusions in the southern Yidun Terrane after Harris et al. (1986). Syn-COLG: syn-collisional granites; WPG: within-plate granites; VAG: volcanic arc granites; PCG: post-collisional granites; LCG: late-collisional granites.
Data for the Relin, Hongshan and Tongchanggou intrusions are from Wang et al. (2014).

(1) Decompression by the late- or post-collisional extension induced upwelling of mantle-derived magmas to underplate in the lower crust, which provided heat for the anatexis of the ancient mafic-intermediate lower crust; (2) The melts, derived from the lower continental crust, mixed with minor mantle-derived magmas; and (3) fractional crystallization generated those Late Cretaceous magmas in the southern Yidun Terrane.

6.4. Geodynamic setting and new constraints on the Late Mesozoic tectonic evolution of the eastern Tibetan Plateau

The Yidun Terrane is a Triassic continental arc located on the east margin of the Qiangtang Terrane (Mo et al., 2001). It originated from westward subduction of the Ganzi–Litang Ocean crust beneath the Zhongza Massif during the Late Triassic (Hou and Mo, 1991). On the basis of a wide distribution of intra-plate magmatism with their ages varying from 189 Ma to 75 Ma, many earlier studies suggested that the Yidun Terrane was under an intra-plate extensional environment during the Jurassic and Cretaceous related to the collision between the Songpan–Ganzi Fold Belt and Yidun Terrane (Hou and Zhou, 2001; Hou et al., 2003, 2004). However, recent zircon LA–ICP-MS U–Pb dating suggests that granites in the Yidun Terrane formed in two periods, i.e. 200–155 Ma and 115–75 Ma (Fig. 14a; Table. 1; Wang et al., 2008b, 2011b, 2014). In addition, not all the later granites (115–75 Ma) are A-type granites. The Relin, Hongshan, and Tongchanggou intrusions are I-type granites with relatively high Sr/Y ratios. Therefore, it is hard to explain how those two periods of granitic magmatism are related to a successive intra-plate extension lasting ca. 114 Ma. Previous studies on Mesozoic cooling across the Yidun Terrane suggested that the Yidun Terrane as a whole had cooled below 300 °C in ca. 200 Ma, which indicates that regional uplifting in the Yidun Terrane occurred later than the Late Triassic Ganzi–Litang oceanic crust subduction events (Reid et al., 2005a, 2005c). In addition, the emplacement of Jurassic intra-plate igneous and associated W–Sn mineralizations in the Yidun Terrane and the west Songpan–Ganzi Fold Belt (Hu et al., 2005; Liu et al., 2007; Qu et al., 2003; Wang et al., 2008b; Zhao et al., 2007) suggest that the sequence of subduction, collision, and intra-plate extension between the Songpan–Ganzi Fold Belt and Yidun Terrane completed during the Late Jurassic. This is also confirmed by the period of magmatic quiescence during ca. 150–120 Ma in those areas (Fig. 14a). Large numbers of apatite fission-track thermochronological studies on rocks (mostly plutons) prior to the Cretaceous in the eastern Tibetan Plateau indicate a Cretaceous (120–80 Ma) cooling and regional uplifting (Fig. 14d; Jolivet et al., 2001; Lai et al., 2007; Reid et al., 2005a; Wang and Wei, 2013; Wilson and Fowler, 2011; Xu and Kamp, 2000; Zheng et al., 2006). Furthermore, a decline in areas of marine sediments in the Qiangtang Terrane and of red bed sediments in the Changdu–Simao Terrane from the Early Jurassic to Late Cretaceous also suggests that regional uplifting happened widely in the eastern Tibetan Plateau during this period (Morley, 2012; Murphy et al., 1997; Yin and Harrison, 2000; Zhang et al., 2012). Therefore, the Yidun Terrane was likely under a collisional uplifting environment during the Late Mesozoic.

As mentioned earlier, the Lhasa Terrane initially collided with the Qiangtang Terrane during the Cretaceous (earlier in the west and later in the east) (Kapp et al., 2005, 2007; Volkmer et al., 2007; Zhu et al., 2013), which probably caused the regional uplifting of the East Tibetan Plateau (ETP). In addition, those widely distributed and compositionally intensified diversity magmatisms (130–110 Ma) in the western Yunnan, Bomi–Chayu region, and northern Lhasa Terrane can be generally explained by the southward subduction of the Bangong Meso-Tethys oceanic crust and the subsequent slab break-off at ca. 113 Ma (Fig. 14b and c; Sui et al., 2013; Xu et al., 2012; Zhu et al., 2009a, 2011b). Then, an intense indention happened between the Lhasa Terrane and Qiangtang Terrane probably during 110–80 Ma (Guynn et al., 2006; Zhang et al., 2012; Zhu et al., 2011a). In this study, the Xiuwacu Late Cretaceous intrusions and the other Late Cretaceous intrusions in the Yidun Terrane probably formed under the late- or post-collision extensional environment (Fig. 13). Their ages, from 115 Ma to 75 Ma, are younger than those of magmas (130–110 Ma) that related to the subduction of the Meso-Tethys in the northern Lhasa Terrane (Fig. 14a and b; Zhu et al., 2009a, 2011a), and are older than those of other magmas that related to the subduction of the Neo-Tethys oceanic crust (80–50 Ma) in the West-Yunnan and Bomi–Chayu region (Fig. 14c; Chiu et al., 2009; Liang et al., 2008; Xu et al., 2012). However, the ages are consistent with the timing of an intense indention between the Lhasa and Qiangtang terranes (110–80 Ma) (Guynn et al., 2006; Zhang et al., 2012; Zhu et al., 2011a). This probably indicates that the tectonic evolution of the Yidun Terrane and the ETP were mainly controlled by the Lhasa–Qiangtang collision during 110–80 Ma. In addition, the Tongchanggou, Hongshan, and Relin intrusions were derived from partial melting of thickened lower crust (Wang et al., 2014), which indicates that the lower crust under the Yidun Terrane was probably thickened prior to the Late Cretaceous in relation to the Lhasa–Qiangtang collision.

As discussed earlier, conclusions regarding when did the Meso-Tethys Ocean close and how long did the Lhasa and Qiangtang collision last remain open to intense debate (Zhang et al., 2012). We compiled 78 apatite fission-track ages of Jurassic granites and sedimentary rocks in the ETP from the published papers. Three identified peak ages (0–10 Ma, 25–45 Ma, and 80–90 Ma) are shown in Fig. 14d. The two younger peak ages probably correspond to the Oligocene (e.g., ~30 Ma ago) and more recent (<7 Ma ago) regional uplift (Wang et al., 2008a). The older peak age of 90–80 Ma also probably corresponds to a gradual regional uplifting event (Fig. 14d; Jolivet et al., 2001; Lai et al., 2007; Reid et al., 2005a; Wang and Wei, 2013; Wilson and Fowler, 2011; Xu and Kamp, 2000; Zheng et al., 2006). Combining with the occurrence of late- or post-collision granites (115–77 Ma) in the ETP (Fig. 14a; Wang et al., 2008b, 2011b, 2014), the timing of both the Lhasa–Qiangtang collision and the ETP uplifting was probably earlier than the Late Cretaceous, and the Lhasa–Qiangtang collision unlikely ceased at least until ca. 80 Ma. In addition, occurrences of large amounts of arc-related magmas from 80 Ma to 50 Ma in the West Yunnan and southern Lhasa Terrane (Fig. 14b and c) and of apatite fission-track ages from 70 Ma to 0 Ma in the ETP (Fig. 14d) indicate that the tectonic setting of the ETP was progressively to be under a control mainly of the tectonic evolution of the Neo-Tethys Ocean and subsequent Indio–Asia collision after ca. 80 Ma.

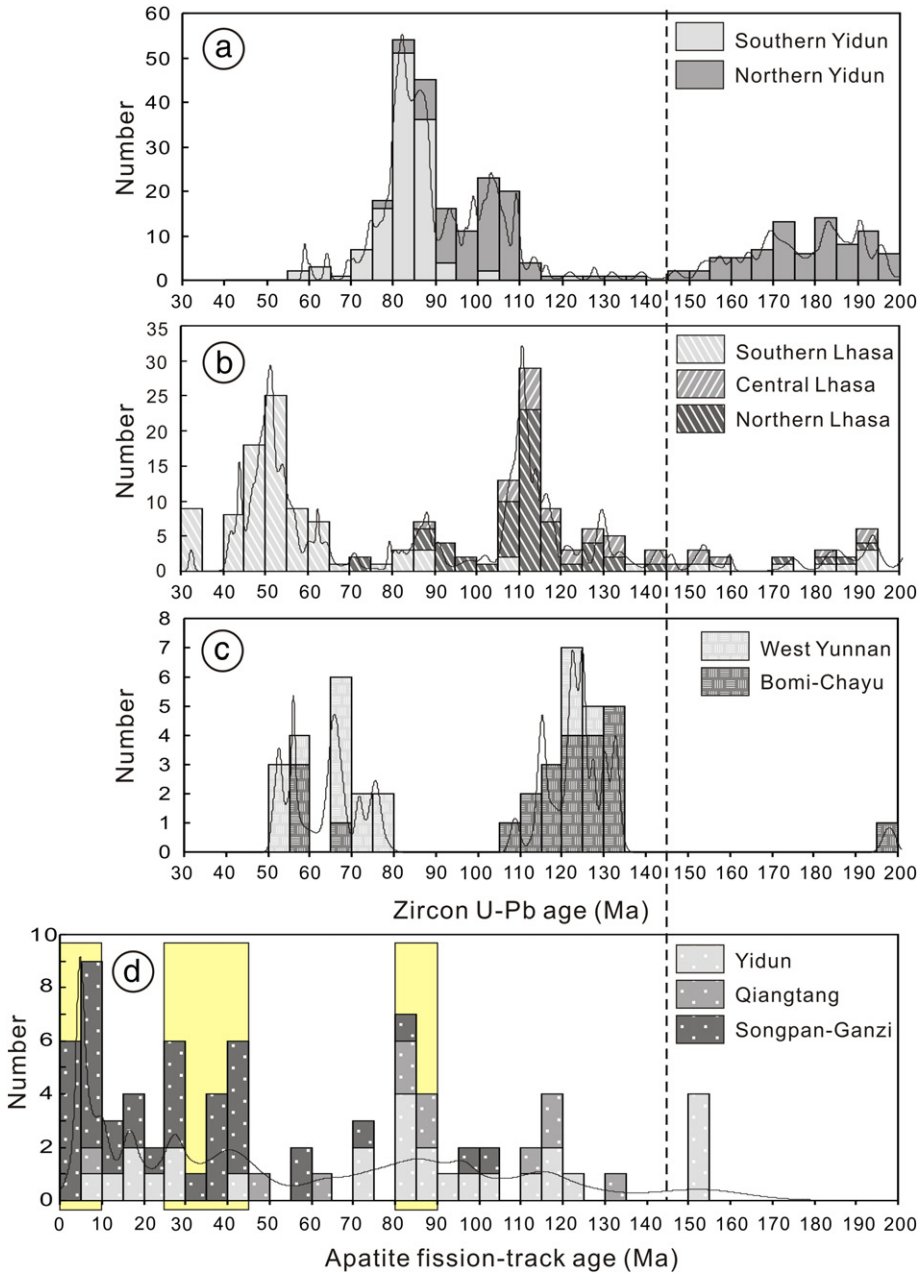

Fig. 14. Histogram of zircon LA–ICP-MS U–Pb ages and apatite fission-track ages for the intrusions in the Lhasa Terrane and East Tibet Plateau. (a) Histogram of single zircon LA–ICP-MS U–Pb ages for the intrusions in the southern Yidun Terrane (Huang et al., 2012; Wang et al., 2008b, 2011b, 2014); (b) and (c) Histogram of zircon LA–ICP-MS U–Pb ages for the intrusions in the Lhasa Terrane, West Yunnan area and Bomi–Chayu region (Chiu et al., 2009; Ji et al., 2009; Kapp et al., 2005, 2007; Lee et al., 2009; Liang et al., 2008; Xu et al., 2012; Zhu et al., 2009a, 2011a); (d) Histogram of apatite fission-track ages for the intrusions in the Yidun Terrane, Qiangtang Terrane and Songpan–Ganzi Fold Belt (Lai et al., 2007; Reid et al., 2005a; Wang and Wei, 2013; Wilson and Fowler, 2011; Xu and Kamp, 2000), the three peak ages (0–10 Ma, 25–45 Ma, and 80–90 Ma) are shown by yellow rectangle.

7. Conclusions

(1) The Xiuwacu Late Cretaceous intrusions consist of three phases with high Si and K, low Mg, Ca, and P, and A/CNK values of 0.95–1.06. They are enriched in Rb, Th, U, and Ta, but depleted in Ba, Sr, P, Ti, and Eu. Furthermore, the intrusions are highly fractionated metaluminous to slightly peraluminous I-type granites, probably with fractional crystallization of Ti-bearing phase (ilmenite, titanite, etc.), apatite, feldspar, and biotite.

(2) The Xiuwacu three phases show similar $\varepsilon_{Nd}(t)$ (−8.0 to −6.9), $(^{87}Sr/^{86}Sr)_i$ (0.7075–0.7098), $\varepsilon_{Hf}(t)$ (−7.6 to −3.2), and $\delta^{18}O$ (5.9‰ to 8.4‰) values, which indicates similar origins. Their Nd–Sr–Hf–O isotopic compositions are also similar with those in the other three contemporary high Sr/Y intrusions in the southern Yidun Terrane. The four intrusions were predominately derived from partial melting of ancient mafic-intermediate thickened lower continental crust with a contribution of mantle components.

(3) The four intrusions in the southern Yidun Terrane were probably generated under a late- or post-collision extensional environment related to the Lhasa–Qiangtang collision during the Late Cretaceous. Occurrence of Late Cretaceous magmas indicates that the timing of both the Lhasa–Qiangtang collision and the eastern Tibetan Plateau uplifting occurred probably earlier than the Late Cretaceous, and that the Lhasa–Qiangtang collision unlikely ceased

until at least ca. 80 Ma. Afterwards, tectonic setting of the eastern Tibetan Plateau was progressively to be under a control mainly of the subduction of the Neo-Tethys Ocean.

Supplementary data to this article can be found online at http://dx.doi.org/10.1016/j.lithos.2014.08.016.

Acknowledgments

This study was jointly supported by the Key Natural Science Foundation of China (41130423), the 12th Five-Year Plan Project of State Key Laboratory of Ore-deposit Geochemistry, Chinese Academy of Sciences (SKLODG-ZY125-03), the CAS/SAFEA International Partnership Program for Creative Research Teams — (Intraplate Mineralization Research Team; KZZD-EW-TZ-20), and the Natural Science Foundation of China (41373051). We would like to thank senior engineer Guang-Hou Yin, Ding-Zhu Huang, and Hai-Jun Yu for their help and fruitful discussion during field investigation, Prof. Zhao-Chu Hu and Prof. Hong-Feng Tang for LA–MC–ICP-MS zircon Hf isotope analyses, Prof. Lian Zhou and Ms. Hong-Mei Gong for whole-rock Sr and Nd isotopes analyes, Prof. Xian-Hua Li, Prof. Qiu-Li Li, Dr. Xiao-Yan Jiang, Mr. Guo-Qiang Tang, and Ms. Hong-Xia Ma for SIMS zircon O isotope analyses, Prof. Liang Qi, Ms. Jing Hu, and Yi-Fan Yin for major and trace elements analyses. Prof. Hong Zhong, Dr. Xun Wei, and Dr. Jiao-Yang Ruan are thanked for discussion with them giving us lots of ideas. Prof. Nelson Eby, Dr. Yongjun Lu, and one anonymous reviewer are very thanked for their constructive and detail reviews of this manuscript.

References

Baker, M.B., Hirschmann, M.M., Ghiorso, M.S., Stolper, E.M., 1995. Compositions of near-solidus peridotite melts from experiments and thermodynamic calculations. Nature 375, 308–311.

Bao, P.S., Xiao, X.C., Su, L., Wang, J., 2007. Petrological, geochemical and chronological constraints for the tectonic setting of the Dongco ophiolite in Tibet. Science in China Series D — Earth Sciences 50, 660–671.

Barbarin, B., 1999. A review of the relationships between granitoid types, their origins and their geodynamic environments. Lithos 46, 605–626.

Barbarin, B., 2005. Mafic magmatic enclaves and mafic rocks associated with some granitoids of the central Sierra Nevada batholith, California: nature, origin, and relations with the hosts. Lithos 80, 155–177.

Barbarin, B., Didier, J., 1992. Genesis and evolution of mafic microgranular enclaves through various types of interaction between coexisting felsic and mafic magmas. Transactions of the Royal Society of Edinburgh: Earth Sciences 83, 145–153.

Chang, C., 1997. Geology and Tectonics of Qinghai–Xizang Plateau Solid Earth Sciences Research in China. Science Press, Beijing 153 pp.

Chappell, B.W., White, A.J.R., 1992. I-type and S-type granites in the Lachlan fold belt. Transactions of the Royal Society of Edinburgh: Earth Sciences 83, 1–26.

Chappell, B.W., White, A.J.R., 2001. Two contrasting granite types: 25 years later. Australian Journal of Earth Sciences 48, 489–499.

Chiaradia, M., 2009. Adakite-like magmas from fractional crystallization and melting-assimilation of mafic lower crust (Eocene Macuchi arc, Western Cordillera, Ecuador). Chemical Geology 265, 468–487.

Chiu, H.Y., Chung, S.L., Wu, F.Y., Liu, D.Y., Liang, Y.H., Lin, I.J., Iizuka, Y., Xie, L.W., Wang, Y.B., Chu, M.F., 2009. Zircon U–Pb and Hf isotopic constraints from eastern Transhimalayan batholiths on the precollisional magmatic and tectonic evolution in southern Tibet. Tectonophysics 477, 3–19.

Collins, W., Beams, S., White, A.J.R., Chappell, B., 1982. Nature and origin of A-type granites with particular reference to southeastern Australia. Contributions to Mineralogy and Petrology 80, 189–200.

Du, D.D., Qu, X.M., Wang, G.H., Xin, H.B., Liu, Z.B., 2011. Bidirectional subduction of the Middle Tethys oceanic basin in the west segment of Bangonghu–Nujiang suture, Tibet: evidence from zircon U–Pb LAICPMS dating and petrogeochemistry of arc granites. Acta Petrologica Sinica 27, 1993–2002.

Eby, G.N., 1990. The A-type granitoids: a review of their occurrence and chemical characteristics and speculations on their petrogenesis. Lithos 26, 115–134.

Ewart, A., Griffin, W.L., 1994. Application of proton-microprobe data to trace-element partitioning in volcanic rocks. Chemical Geology 117, 251–284.

Frost, B.R., Barnes, C.G., Collins, W.J., Arculus, R.J., Ellis, D.J., Frost, C.D., 2001. A geochemical classification for granitic rocks. Journal of Petrology 42, 2033.

Gao, S., Ling, W.L., Qiu, Y.M., Lian, Z., Hartmann, G., Simon, K., 1999. Contrasting geochemical and Sm–Nd isotopic compositions of Archean metasediments from the Kongling high-grade terrain of the Yangtze craton: evidence for cratonic evolution and redistribution of REE during crustal anatexis. Geochimica et Cosmochimica Acta 63, 2071–2088.

Green, D., 1973. Experimental melting studies on a model upper mantle composition at high pressure under water-saturated and water-undersaturated conditions. Earth and Planetary Science Letters 19, 37–53.

Griffin, W.L., Wang, X., Jackson, S.E., Pearson, N.J., O'Reilly, S.Y., Xu, X.S., Zhou, X.M., 2002. Zircon chemistry and magma mixing, SE China: in-situ analysis of Hf isotopes, Tonglu and Pingtan igneous complexes. Lithos 61, 237–269.

Guynn, J.H., Kapp, P., Pullen, A., Heizier, M., Gehrels, G., Ding, L., 2006. Tibetan basement rocks near Amdo reveal "missing" Mesozoic tectonism along the Bangong suture, central Tibet. Geology 34, 505–508.

Harris, N.B., Pearce, J.A., Tindle, A.G., 1986. Geochemical characteristics of collision-zone magmatism. Geological Society, London, Special Publications 19, 67–81.

He, D.F., Zhu, W.G., Zhong, H., Ren, T., Bai, Z.J., Fan, H.P., 2013. Zircon U–Pb geochronology and elemental and Sr–Nd–Hf isotopic geochemistry of the Daocheng granitic pluton from the Yidun Arc, SW China. Journal of Asian Earth Sciences 67–68, 1–17.

Hofmann, A.W., 2003. Sampling mantle heterogeneity through oceanic basalts: isotopes and trace elements. Treatise on Geochemistry 2, 61–101.

Hou, Z.Q., Mo, X.X., 1991. A tectono-magmatic evolution of Yidun island arc in Sanjiang region, China. Contribution to the Geology of the Qinghai–Xizang (Tibet). Plateau 153–165 (in Chinese).

Hou, Z.Q., Zhou, J.R., 2001. Collision-orogenic processes of the Yidun Arc in the Sanjiang region: record of granites. Acta Geologica Sinica 75, 484–497 (in Chinese with English abstract).

Hou, Z.Q., Yang, Y.Q., Wang, H.P., Qu, X.M., Lv, Q.T., Huang, D.H., Wu, X.Z., Yu, J.J., Tang, S.H., Zhao, J.H., 2003. Collision-Orogenic Progress and Mineralization System of Yidun Arc. Geological Publishing House, Beijing 335 pp.; (in Chinese).

Hou, Z.Q., Yang, Y.Q., Qu, X.M., Huang, D.H., Lu, Q.T., Wang, H.P., Yu, J.J., Tang, S.H., 2004. Tectonic evolution and mineralization systems of the Yidun Arc orogen in Sanjiang region, China. Acta Geologica Sinica 78, 109–120 (in Chinese with English abstract).

Hou, Z.Q., Zaw, K., Pan, G.T., Mo, X.X., Xu, Q., Hu, Y.Z., Li, X.Z., 2007. Sanjiang Tethyan metallogenesis in SW China: tectonic setting, metallogenic epochs and deposit types. Ore Geology Reviews 31, 48–87.

Hou, Z.Q., Zheng, Y.C., Yang, Z.M., Rui, Z.Y., Zhao, Z.D., Jiang, S.H., Qu, X.M., Sun, Q.Z., 2013. Contribution of mantle components within juvenile lower-crust to collisional zone porphyry Cu systems in Tibet. Mineralium Deposita 48, 173–192.

Hu, J.M., Meng, Q.R., Shi, Y.R., Qu, H.J., 2005. SHRIMP U–Pb dating of zircons from granitoid bodies in the Songpan–Ganzi terrane and its implications. Acta Petrologica Sinica 21, 867–880.

Hu, Z.C., Gao, S., Liu, Y.S., Hu, S.H., Chen, H.H., Yuan, H.L., 2008a. Signal enhancement in laser ablation ICP-MS by addition of nitrogen in the central channel gas. Journal of Analytical Atomic Spectrometry 23, 1093–1101.

Hu, Z.C., Liu, Y.S., Gao, S., Hu, S.H., Dietiker, R., Günther, D., 2008b. A local aerosol extraction strategy for the determination of the aerosol composition in laser ablation inductively coupled plasma mass spectrometry. Journal of Analytical Atomic Spectrometry 23, 1192–1203.

Hu, Z.C., Liu, Y.S., Gao, S., Liu, W.G., Zhang, W., Tong, X.R., Lin, L., Zong, K.Q., Li, M., Chen, H.H., 2012a. Improved in situ Hf isotope ratio analysis of zircon using newly designed X skimmer cone and jet sample cone in combination with the addition of nitrogen by laser ablation multiple collector ICP-MS. Journal of Analytical Atomic Spectrometry 27, 1391–1399.

Hu, Z.C., Liu, Y.S., Gao, S., Xiao, S.Q., Zhao, L.S., Günther, D., Li, M., Zhang, W., Zong, K.Q., 2012b. A "wire" signal smoothing device for laser ablation inductively coupled plasma mass spectrometry analysis. Spectrochimica Acta Part B: Atomic Spectroscopy 78, 50–57.

Huang, X.X., Xu, J.F., Chen, J.L., Ren, J.B., 2012. Geochronology, geochemistry and petrogenesis of two periods of intermediate-acid intrusive rocks from Hongshan area in Zhongdian arc. Acta Petrologica Sinica 28, 1493–1506.

Jahn, B.M., Wu, F.Y., Lo, C.H., Tsai, C.H., 1999. Crust–mantle interaction induced by deep subduction of the continental crust: Geochemical and Sr–Nd isotopic evidence from post-collisional mafic–ultramafic intrusions of the northern Dabie complex, central China. Chemical Geology 157, 119–146.

Ji, W.Q., Wu, F.Y., Chung, S.L., Li, J.X., Liu, C.Z., 2009. Zircon U–Pb geochronology and Hf isotopic constraints on petrogenesis of the Gangdese batholith, southern Tibet. Chemical Geology 262, 229–245.

Jolivet, M., Brunel, M., Seward, D., Xu, Z., Yang, J., Roger, F., Tapponnier, P., Malavieille, J., Arnaud, N., Wu, C., 2001. Mesozoic and Cenozoic tectonics of the northern edge of the Tibetan Plateau: fission-track constraints. Tectonophysics 343, 111–134.

Kapp, P., Murphy, M.A., Yin, A., Harrison, T.M., Ding, L., Guo, J.H., 2003. Mesozoic and Cenozoic tectonic evolution of the Shiquanhe area of western Tibet. Tectonics 22.

Kapp, P., Yin, A., Harrison, T.M., Ding, L., 2005. Cretaceous–Tertiary shortening, basin development, and volcanism in central Tibet. Geological Society of America Bulletin 117, 865–878.

Kapp, P., DeCelles, P.G., Gehrels, G.E., Heizier, M., Ding, L., 2007. Geological records of the Lhasa–Qiangtang and Indo–Asian collisions in the Nima area of central Tibet. Geological Society of America Bulletin 119, 917–932.

Keay, S., Collins, W.J., McCulloch, M.T., 1997. A three-component Sr–Nd isotopic mixing model for granitoid genesis, Lachlan fold belt, eastern Australia. Geology 25, 307–310.

Kemp, A.I.S., Wormald, R.J., Whitehouse, M.J., Price, R.C., 2005. Hf isotopes in zircon reveal contrasting sources and crystallization histories for alkaline to peralkaline granites of Temora, southeastern Australia. Geology 33, 797–800.

Kemp, A.I.S., Hawkesworth, C.J., Foster, G.L., Paterson, B.A., Woodhead, J.D., Hergt, J.M., Gray, C.M., Whitehouse, M.J., 2007. Magmatic and crustal differentiation history of granitic rocks from Hf–O isotopes in zircon. Science 315, 980–983.

Kempton, P.D., Harmon, R.S., 1992. Oxygen isotope evidence for large-scale hybridization of the lower crust during magmatic underplating. Geochimica et Cosmochimica Acta 56, 971–986.

Keto, L.S., Jacobsen, S.B., 1987. Nd and Sr isotopic variations of Early Paleozoic oceans. Earth and Planetary Science Letters 84, 27–41.

Lai, Q.Z., Ding, L., Wang, H.W., Yue, Y.H., Cai, F.L., 2007. Constraining the stepwise migration of the eastern Tibetan Plateau margin by apatite fission track thermochronology. Science in China Series D — Earth Sciences 50, 172–183.
Lee, H.Y., Chung, S.L., Lo, C.H., Ji, J.Q., Lee, T.Y., Qian, Q., Zhang, Q., 2009. Eocene Neotethyan slab breakoff in southern Tibet inferred from the Linzizong volcanic record. Tectonophysics 477, 20–35.
Leng, C.B., Zhang, X.C., Hu, R.Z., Wang, S.X., Zhong, H., Wang, W.Q., Bi, X.W., 2012. Zircon U–Pb and molybdenite Re–Os geochronology and Sr–Nd–Pb–Hf isotopic constraints on the genesis of the Xuejiping porphyry copper deposit in Zhongdian, Northwest Yunnan, China. Journal of Asian Earth Sciences 60, 31–48.
Leng, C.B., Huang, Q.Y., Zhang, X.C., Wang, S.X., Zhong, H., Hu, R.Z., Bi, X.W., Zhu, J.J., Wang, X.S., 2014. Petrogenesis of the Late Triassic volcanic rocks in the Southern Yidun arc, SW China: constraints from the geochronology, geochemistry, and Sr–Nd–Pb–Hf isotopes. Lithos 190, 363–382.
Li, J.K., Li, W.C., Wang, D.H., Lu, Y.X., Yin, G.H., Xue, S.R., 2007a. Re–Os dating for ore-forming event in the late of Yanshan Epoch and research of ore-forming regularity in Zhongdian Arc. Acta Petrologica Sinica 23, 2415–2422.
Li, X.H., Li, Z.X., Li, W.X., Liu, Y., Yuan, C., Wei, G.J., Qi, C.S., 2007b. U–Pb zircon, geochemical and Sr–Nd–Hf isotopic constraints on age and origin of Jurassic I- and A-type granites from central Guangdong, SE China: a major igneous event in response to foundering of a subducted flat-slab? Lithos 96, 186–204.
Li, J.W., Zhao, X.F., Zhou, M.F., Ma, C.Q., de Souza, Z.S., Vasconcelos, P., 2009a. Late Mesozoic magmatism from the Daye region, eastern China: U–Pb ages, petrogenesis, and geodynamic implications. Contributions to Mineralogy and Petrology 157, 383–409.
Li, X.H., Li, W.X., Wang, X.C., Li, Q.L., Liu, Y., Tang, G.Q., 2009b. Role of mantle-derived magma in genesis of early Yanshanian granites in the Nanling Range, South China: in situ zircon Hf–O isotopic constraints. Science in China, Series D: Earth Sciences 52, 1262–1278.
Li, X.H., Li, W.X., Li, Q.L., Wang, X.C., Liu, Y., Yang, Y.H., 2010a. Petrogenesis and tectonic significance of the similar to 850 Ma Gangbian alkaline complex in South China: evidence from in situ zircon U–Pb dating, Hf–O isotopes and whole-rock geochemistry. Lithos 114, 1–15.
Li, X.H., Long, W.G., Li, Q.L., Liu, Y., Zheng, Y.F., Yang, Y.H., Chamberlain, K.R., Wan, D.F., Guo, C.H., Wang, X.C., 2010b. Penglai zircon megacrysts: a potential new working reference material for microbeam determination of Hf–O isotopes and U–Pb age. Geostandards and Geoanalytical Research 34, 117–134.
Li, J.X., Qin, K.Z., Li, G.M., Xiao, B., Zhao, J.X., Cao, M.J., Chen, L., 2013a. Petrogenesis of ore-bearing porphyries from the Duolong porphyry Cu–Au deposit, central Tibet: evidence from U–Pb geochronology, petrochemistry and Sr–Nd–Hf–O isotope characteristics. Lithos 160–161, 216–227.
Li, X.H., Tang, G.Q., Guo, B., Yang, Y.H., Hou, K.J., Hu, Z.C., Li, Q.L., Liu, Y., Li, W.X., 2013b. Qinghu zircon: a working reference for microbeam analysis of U–Pb age and Hf and O isotopes. Chinese Science Bulletin 36, 4647–4654.
Liang, Y.H., Chung, S.L., Liu, D.Y., Xu, Y.G., Wu, F.Y., Yang, J.H., Wang, Y., Lo, C.H., 2008. Detrital zircon evidence from Burma for reorganization of the eastern Himalayan river system. American Journal of Science 308, 618–638.
Liu, Y., Deng, J., Li, C.F., Shi, G.H., Zheng, A.L., 2007. REE composition in scheelite and scheelite Sm–Nd dating for the Xuebaoding W–Sn–Be deposit in Sichuan. Chinese Science Bulletin 52, 2543–2550.
Lu, Y.J., Kerrich, R., McCuaig, T.C., Li, Z.X., Hart, C.J.R., Cawood, P.A., Hou, Z.Q., Bagas, L., Cliff, J., Belousova, E.A., Tang, S.H., 2013. Geochemical, Sr–Nd–Pb, and zircon Hf–O isotopic compositions of Eocene–Oligocene shoshonitic and potassic adakite-like felsic intrusions in western Yunnan, SW China: petrogenesis and tectonic implications. Journal of Petrology 54, 1309–1348.
Ma, C.Q., Ehlers, C., Xu, C.H., Li, Z.C., Yang, K.G., 2000. The roots of the Dabieshan ultrahigh-pressure metamorphic terrane: constraints from geochemistry and Nd–Sr isotope systematics. Precambrian Research 102, 279–301.
Maniar, P.D., Piccoli, P.M., 1989. Tectonic discrimination of granitoids. Bulletin of the Geological Society of America 101, 635.
Metcalfe, I., 2011. Tectonic framework and Phanerozoic evolution of Sundaland. Gondwana Research 19, 3–21.
Middlemost, E.A.K., 1994. Naming materials in the magma/igneous rock system. Earth-Science Reviews 37, 215–224.
Mo, X.X., Deng, J.F., Dong, F.L., H., Y.X., Wang, Y., Zhou, S., Yang, W.G., 2001. Volcanic petrotectonic assemblages in Sanjiang Orogenic Belt, SW China and implication for tectonics. Geological Journal of China Universities 7, 121–138 (in Chinese with English abstract).
Morley, C.K., 2012. Late Cretaceous–Early Palaeogene tectonic development of SE Asia. Earth-Science Reviews 115, 37–75.
Murphy, M.A., Yin, A., Harrison, T.M., Dürr, S.B., Chen, Z., Ryerson, F.J., Kidd, W.S.F., Wang, X., Zhou, X., 1997. Did the Indo–Asian collision alone create the Tibetan Plateau? Geology 25, 719–722.
Pan, G.T., Wang, L.Q., Li, R.S., Yuan, S.H., Ji, W.H., Yin, F.G., Zhang, W.P., Wang, B.D., 2012. Tectonic evolution of the Qinghai–Tibet Plateau. Journal of Asian Earth Sciences 53, 3–14.
Qi, L., Hu, J., Gregoire, D.C., 2000. Determination of trace elements in granites by inductively coupled plasma mass spectrometry. Talanta 51, 507–513.
Qu, X.M., Hou, Z.Q., Zhou, S.G., 2002. Geochemical and Nd, Sr isotopic study of the post-orogenic granites in the Yidun arc belt of northern Sanjiang region, southwestern China. Resource Geology 52, 163–172.
Qu, X.M., Hou, Z.Q., Tang, S.H., 2003. Age of intraplate volcanism in the back-arc area of Yidun island arc and its significance. Petrologica et Mineralogica 22, 131–137 (in Chinese with English abstract).
Qu, X.M., Wang, R.J., Xin, H.B., Jiang, J.H., Chen, H., 2012. Age and petrogenesis of A-type granites in the middle segment of the Bangonghu–Nujiang suture, Tibetan Plateau. Lithos 146, 264–275.
Reid, A.J., Fowler, A.P., Phillips, D., Wilson, C.J.L., 2005a. Thermochronology of the Yidun Arc, central eastern Tibetan Plateau: constraints from (40)Ar/(39)Ar K-feldspar and apatite fission track data. Journal of Asian Earth Sciences 25, 915–935.
Reid, A.J., Wilson, C.J.L., Liu, S., 2005b. Structural evidence for the Permo-Triassic tectonic evolution of the Yidun Arc, eastern Tibetan Plateau. Journal of Structural Geology 27, 119–137.
Reid, A.J., Wilson, C.J.L., Phillips, D., Liu, S., 2005c. Mesozoic cooling across the Yidun Arc, central-eastern Tibetan Plateau: a reconnaissance Ar-40/Ar-39 study. Tectonophysics 398, 45–66.
Reid, A., Wilson, C.J.L., Shun, L., Pearson, N., Belousova, E., 2007. Mesozoic plutons of the Yidun Arc, SW China: U/Pb geochronology and Hf isotopic signature. Ore Geology Reviews 31, 88–106.
Richards, J.R., Kerrich, R., 2007. Special paper: adakite-like rocks: their diverse origins and questionable role in metallogenesis. Economic Geology 102, 537–576.
Sengor, A.M.C., 1979. Mid-Mesozoic closure of Permo-Triassic Tethys and its implications. Nature 279, 590–593.
Sengor, A.M.C., 1987. Tectonics of the Tethysides-orogenic collage development in a collisional setting. Annual Review of Earth and Planetary Sciences 15, 213–244.
Sui, Q.L., Wang, Q., Zhu, D.C., Zhao, Z.D., Chen, Y., Santosh, M., Hu, Z.C., Yuan, H.L., Mo, X.X., 2013. Compositional diversity of ca. 110 Ma magmatism in the northern Lhasa Terrane, Tibet: implications for the magmatic origin and crustal growth in a continent–continent collision zone. Lithos 168, 144–159.
Sun, S.S., McDonough, W.F., 1989. Chemical and isotopic systematics of oceanic basalts: implications for mantle composition and processes. Geological Society, London, Special Publications 42, 313–345.
Sylvester, P.J., 1998. Post-collisional strongly peraluminous granites. Lithos 45, 29–44.
Valley, J.W., Lackey, J.S., Cavosie, A.J., Clechenko, C.C., Spicuzza, M.J., Basei, M.A.S., Bindeman, I.N., Ferreira, V.P., Sial, A.N., King, E.M., Peck, W.H., Sinha, A.K., Wei, C.S., 2005. 4.4 billion years of crustal maturation: oxygen isotope ratios of magmatic zircon. Contributions to Mineralogy and Petrology 150, 561–580.
Volkmer, J.E., Kapp, P., Guynn, J.H., Lai, Q.Z., 2007. Cretaceous–Tertiary Structural Evolution of the North Central Lhasa Terrane, Tibet. Tectonics 26.
Wang, L.C., Wei, Y.S., 2013. Apatite fission track thermochronology evidence for the Mid-Cretaceous tectonic event in the Qiangtang Basin, Tibet. Acta Petrologica Sinica 29, 1039–1047.
Wang, C.S., Zhao, X.X., Liu, Z.F., Lippert, P.C., Graham, S.A., Coe, R.S., Yi, H.S., Zhu, L.D., Liu, S., Li, Y.L., 2008a. Constraints on the early uplift history of the Tibetan Plateau. Proceedings of the National Academy of Sciences of the United States of America 105, 4987–4992.
Wang, Q.W., Wang, K.M., Han, Z.Z., Fu, X.F., Liang, B., Yao, Z.D., Dai, Z.M., Luo, S.L., Zhong, C.H., Wei, Y.F., 2008b. The Granite in West Sichuan and its Metallogenic Series. Geological Publishing House, Beijing 305 pp.; (in Chinese).
Wang, B.Q., Zhou, M.F., Li, J.W., Yan, D.P., 2011a. Late Triassic porphyritic intrusions and associated volcanic rocks from the Shangri-La region, Yidun terrane, Eastern Tibetan Plateau: adakitic magmatism and porphyry copper mineralization. Lithos 127, 24–38.
Wang, X.S., Bi, X.W., Leng, C.B., Tang, Y.Y., Lan, J.B., Qi, Y.Q., Shen, N.P., 2011b. LA–ICP-MS zircon U–Pb dating of granite porphyry in the Hongshan Cu–polymetallic deposit, Zhongdian, northwest Yunnan, China and its geological implication. Acta Mineralogica Sinica 31, 315–321 (in Chinese with English abstract).
Wang, B.Q., Wang, W., Chen, W.T., Gao, J.F., Zhao, X.F., Yan, D.P., Zhou, M.F., 2013. Constraints of detrital zircon U–Pb ages and Hf isotopes on the provenance of the Triassic Yidun Group and tectonic evolution of the Yidun Terrane, Eastern Tibet. Sedimentary Geology 289, 74–98.
Wang, X.S., Bi, X.W., Leng, C.B., Zhong, H., Tang, H.F., Chen, Y.W., Yin, G.H., Huang, D.Z., Zhou, M.F., 2014. Geochronology and geochemistry of Late Cretaceous igneous intrusions and Mo–Cu–(W) mineralization in the southern Yidun Arc, SW China: implications for metallogenesis and geodynamic setting. Ore Geology Reviews 61, 73–95.
Whalen, J.B., Currie, K.L., Chappell, B.W., 1987. A-type granites: geochemical characteristics, discrimination and petrogenesis. Contributions to Mineralogy and Petrology 95, 407–419.
Wilson, C.J.L., Fowler, A.P., 2011. Denudational response to surface uplift in east Tibet: evidence from apatite fission-track thermochronology. Geological Society of America Bulletin 123, 1966–1987.
Woodhead, J., Hergt, J., Shelley, M., Eggins, S., Kemp, R., 2004. Zircon Hf-isotope analysis with an excimer laser, depth profiling, ablation of complex geometries, and concomitant age estimation. Chemical Geology 209, 121–135.
Wu, F.Y., Sun, D.Y., Li, H.M., Jahn, B.M., Wilde, S., 2002. A-type granites in northeastern China: age and geochemical constraints on their petrogenesis. Chemical Geology 187, 143–173.
Wu, F.Y., Jahn, B.M., Wilde, S.A., Lo, C.H., Yui, T.F., Lin, Q., Ge, W.C., Sun, D.Y., 2003a. Highly fractionated I-type granites in NE China (I): geochronology and petrogenesis. Lithos 66, 241–273.
Wu, F.Y., Jahn, B.M., Wilde, S.A., Lo, C.H., Yui, T.F., Lin, Q., Ge, W.C., Sun, D.Y., 2003b. Highly fractionated I-type granites in NE China (II): isotopic geochemistry and implications for crustal growth in the Phanerozoic. Lithos 67, 191–204.
Wu, W.H., Xu, S.J., Yang, J.D., Yin, H.W., Lu, H.Y., Zhang, K.J., 2010. Isotopic characteristics of river sediments on the Tibetan Plateau. Chemical Geology 269, 406–413.
Xu, J.F., Castillo, P.R., 2004. Geochemical and Nd–Pb isotopic characteristics of the Tethyan asthenosphere: implications for the origin of the Indian Ocean mantle domain. Tectonophysics 393, 9–27.
Xu, G.Q., Kamp, P.J.J., 2000. Tectonics and denudation adjacent to the Xianshuihe Fault, eastern Tibetan Plateau: constraints from fission track thermochronology. Journal of Geophysical Research: Solid Earth 105, 19231–19251 (1978–2012).
Xu, Y.G., Yang, Q.J., Lan, J.B., Luo, Z.Y., Huang, X.L., Shi, Y.R., Xie, L.W., 2012. Temporal–spatial distribution and tectonic implications of the batholiths in the Gaoligong–Tengliang–Yingjiang area, western Yunnan: constraints from zircon U–Pb ages and Hf isotopes. Journal of Asian Earth Sciences 53, 151–175.

Yang, J.H., Wu, F.Y., Chung, S.L., Wilde, S.A., Chu, M.F., 2004. Multiple sources for the origin of granites: geochemical and Nd/Sr isotopic evidence from the Gudaoling granite and its mafic enclaves, northeast China. Geochimica et Cosmochimica Acta 68, 4469–4483.

Yang, J.H., Wu, F.Y., Chung, S.L., Wilde, S.A., Chu, M.F., 2006. A hybrid origin for the Qianshan A-type granite, northeast China: geochemical and Sr–Nd–Hf isotopic evidence. Lithos 89, 89–106.

Yin, A., Harrison, T.M., 2000. Geologic evolution of the Himalayan–Tibetan orogen. Annual Review of Earth and Planetary Sciences 28, 211–280.

Ying, H.L., Wang, D.H., Fu, X.F., 2006. Timing and lead and sulfur isotope composition of Xiasai granite and silver polymetallic deposit in Batang, Sichuan Province. Mineral Deposits 25, 136–146 (in Chinese with English abstract).

Zeng, P.S., Mo, X.X., Yu, Y.H., Hou, Z.Q., Xu, Q.D., Wang, H.P., Li, H., Yang, C.Z., 2003. Porphyries and porphyry copper deposits in Zhongdian area, northwestern Yunnan. Mineral Deposits 22, 393–400 (in Chinese with English abstract).

Zhang, N.D., 1994. Age of granitoids in Baiyu–Daocheng region, west Sichuan. Acta Geologica Sichuan 14, 88–99 (in Chinese with English abstract).

Zhang, N.D., Zhang, H.J., 1993. Ages of several granite plutons in northwestern Sichuan. Geochimica 303–312 (in Chinese with English abstract).

Zhang, S.B., Zheng, Y.F., Wu, Y.B., Zhao, Z.F., Gao, S., Wu, F.Y., 2006. Zircon U–Pb age and Hf–O isotope evidence for Paleoproterozoic metamorphic event in South China. Precambrian Research 151, 265–288.

Zhang, K.J., Zhang, Y.X., Tang, X.C., Xia, B., 2012. Late Mesozoic tectonic evolution and growth of the Tibetan Plateau prior to the Indo–Asian collision. Earth-Science Reviews 114, 236–249.

Zhao, Y.J., Yuan, C., Zhou, M.F., Yan, D.P., Long, X.P., Cai, K.D., 2007. Post-orogenic extension of Songpan–Garzê orogen in Early Jurassic: constraints from Niuxingou monzodiorite and Siguniangshan A-type granite of western Sichuan, China. Geochemica 36, 139–142 (in Chinese with English abstract).

Zheng, D.W., Zhang, P.Z., Wan, J.L., Yuan, D.Y., Li, C.Y., Yin, G.M., Zhang, G.L., Wang, Z.C., Min, W., Chen, J., 2006. Rapid exhumation at similar to 8 Ma on the Liupan Shan thrust fault from apatite fission-track thermochronology: implications for growth of the northeastern Tibetan Plateau margin. Earth and Planetary Science Letters 248, 198–208.

Zhong, H., Zhu, W.G., Hu, R.Z., Xie, L.W., He, D.F., Liu, F., Chu, Z.Y., 2009. Zircon U–Pb age and Sr–Nd–Hf isotope geochemistry of the Panzhihua A-type syenitic intrusion in the Emeishan large igneous province, southwest China and implications for growth of juvenile crust. Lithos 110, 109–128.

Zhou, L., Gao, S., Liu, Y.S., Ling, W.L., Zhang, L., 2007. Geochemistry and implications of clastic sedimentary rocks from the northern margin of Yangtze Craton. Earth Science—Journal of China University of Geosciences 32, 29–38.

Zhu, D.C., Mo, X.X., Niu, Y.L., Zhao, Z.D., Wang, L.Q., Liu, Y.S., Wu, F.Y., 2009a. Geochemical investigation of Early Cretaceous igneous rocks along an east–west traverse throughout the central Lhasa Terrane, Tibet. Chemical Geology 268, 298–312.

Zhu, D.C., Mo, X.X., Wang, L.Q., Zhao, Z.D., Niu, Y.L., Zhou, C.Y., Yang, Y.H., 2009b. Petrogenesis of highly fractionated I-type granites in the Zayu area of eastern Gangdese, Tibet: constraints from zircon U–Pb geochronology, geochemistry and Sr–Nd–Hf isotopes. Science in China Series D — Earth Sciences 52, 1223–1239.

Zhu, D.C., Zhao, Z.D., Niu, Y.L., Mo, X.X., Chung, S.L., Hou, Z.Q., Wang, L.Q., Wu, F.Y., 2011a. The Lhasa Terrane: record of a microcontinent and its histories of drift and growth. Earth and Planetary Science Letters 301, 241–255.

Zhu, J.L., Hu, R.Z., Bi, X.W., Zhong, H., Chen, H., 2011b. Zircon U–Pb ages, Hf–O isotopes and whole-rock Sr–Nd–Pb isotopic geochemistry of granitoids in the Jinshajiang suture zone, SW China: constraints on petrogenesis and tectonic evolution of the Paleo-Tethys Ocean. Lithos 126, 248–264.

Zhu, D.C., Zhao, Z.D., Niu, Y.L., Dilek, Y., Hou, Z.Q., Mo, X.X., 2013. The origin and pre-Cenozoic evolution of the Tibetan Plateau. Gondwana Research 23, 1429–1454.